

Novel adsorbent synthesized from red mud and acid mine drainage for enhanced contaminant removal: industrial waste transformation, adsorbent performance and metal(loid) removal mechanisms

Zhang, D-R., Chen, H-R., Xia, J-L., Nie, Z-Y., Zhao, X-J. & Pakostova, E

Author post-print (accepted) deposited by Coventry University's Repository

Original citation & hyperlink:

Zhang, D-R, Chen, H-R, Xia, J-L, Nie, Z-Y, Zhao, X-J & Pakostova, E 2023, 'Novel adsorbent synthesized from red mud and acid mine drainage for enhanced contaminant removal: industrial waste transformation, adsorbent performance and metal(loid) removal mechanisms', Chemical Engineering Journal, vol. 465, 142867.

<https://doi.org/10.1016/j.cej.2023.142867>

DOI 10.1016/j.cej.2023.142867

ISSN 1385-8947

Publisher: Elsevier

© 2023, Elsevier. Licensed under the Creative Commons Attribution-NonCommercial-NoDerivatives 4.0 International

<http://creativecommons.org/licenses/by-nc-nd/4.0/>

Copyright © and Moral Rights are retained by the author(s) and/ or other copyright owners. A copy can be downloaded for personal non-commercial research or study, without prior permission or charge. This item cannot be reproduced or quoted extensively from without first obtaining permission in writing from the copyright holder(s). The content must not be changed in any way or sold commercially in any format or medium without the formal permission of the copyright holders.

This document is the author's post-print version, incorporating any revisions agreed during the peer-review process. Some differences between the published version and this version may remain and you are advised to consult the published version if you wish to cite from it.

**Novel adsorbent synthesized from red mud and acid mine drainage
for enhanced contaminant removal: industrial waste transformation,
adsorbent performance and metal(loid) removal mechanisms**

Duo-Rui Zhang^{a,b,1}, Hong-Rui Chen^{a,b,1}, Jin-Lan Xia^{a,b,*}, Zhen-Yuan Nie^{a,b,*}, Xiao-Juan Zhao^c,
Eva Pakostova^d

^a School of Minerals Processing and Bioengineering, Central South University, Changsha 410083, China

^b Key Lab of Biometallurgy of Ministry of Education of China, Central South University, Changsha 410083, China

^c Beijing Synchrotron Radiation Facility, Institute of High Energy Physics, Chinese Academy of Sciences, Beijing 100049, China

^d Centre for Manufacturing and Materials, Coventry University, Coventry CV1 5FB, UK

*Corresponding author: e-mail: jlxia@csu.edu.cn; zynie@csu.edu.cn

¹ The authors contributed equally to the work.

Abstract: Antimony (Sb), arsenic (As), and lead (Pb) are toxic metal(loid)s that can cause serious environmental pollution. The above emphasizes the need for a development of efficient technologies for metal(loid) removal, especially from low-pH environments due to the increased mobility of the contaminants under acidic conditions. Herein, for the first time, removal of Sb(V/III), As(V/III), and Pb(II) from acidic waters is described, using low-cost adsorbents synthesized from red mud (RM; a solid waste from the alumina industry) under the catalysis by acid mine drainage (AMD; acidic effluents from mines). The reactions between RM and AMD were studied to describe Fe/S/Ca/Al/Si speciation transformations during the adsorbent formation. In addition, Sb/As/Pb adsorption behavior and the relationship between adsorbent properties and Sb/As/Pb removal efficiencies were investigated. The maximum removal capacities for Sb(V), Sb(III), As(V), As(III), and Pb(II) reaching 1,637.8, 80.2, 109.2, 16.4, and 518.7 mg/g, respectively. The primarily Ca^{2+} from the Ca-bearing compounds (determined in RA2, synthesized under $S_{\text{RM}}/L_{\text{AMD}}$ 2:1) contributed to Sb(V) removal (*via* precipitation of $\text{CaSb}_2\text{O}_5(\text{OH})_2$ and formation of Sb-bearing precipitate, with silicate gel nanospheres securing high stability of the immobilized Sb). In the As immobilization process, Fe(III) (hydr)oxides (formed in RA4, synthesized under $S_{\text{RM}}/L_{\text{AMD}}$ 4:1) such as goethite (α - FeOOH) and bernalite ($\text{Fe}(\text{OH})_3$) played a dominant role. Convertible sulfates (e.g., CaSO_4 and $\text{Al}_2(\text{SO}_4)_3$) in RA10 (synthesized under $S_{\text{RM}}/L_{\text{AMD}}$ 10:1) ensured a high removal capacity for Pb(II) across a wide pH range (2 to 7) via PbSO_4 precipitation. In contrast, the formation of PbCO_3 and $\text{Pb}_3(\text{CO}_3)_2(\text{OH})_2$ was the main mechanism for Pb(II) removal by unamended RM at pH 5.0, while no contaminant removal capacity was observed at pH 2.0.

Keywords: Metal(loid) contaminant removal; Red mud; Acid mine drainage; Adsorption; Waste utilization; Low-cost adsorbent

1. Introduction

Elevated concentrations of antimony (Sb), arsenic (As), and Pb in soils and waters, originating from both natural geological processes and anthropogenic activities (e.g., industrial emissions and mining activities), can be harmful to the environment and human health [1,2]. The US EPA, EU, and World Health Organization have all adopted 5 $\mu\text{g/L}$ for Sb and 10 $\mu\text{g/L}$ for As and Pb as legal standards in drinking water [3]. Elevated levels of Sb ($> 10 \mu\text{g/L}$) have been detected in an increasing number of places, particularly in the soils and rivers near Sb mines [4], and Pb(II) concentrations up to 15,

250, and 920 $\mu\text{g/L}$ have been reported in drinking water [5], groundwater [6], and wastewater [7], respectively. Many countries around the world have been affected by As contamination of water bodies, with concentrations typically ranging from 1 $\mu\text{g/L}$ to 10 mg/L [8], but reaching up to 30 mg/L of As was in highly polluted acidic nonferrous smelting wastewaters [9]. Due to the above, it is important that cost-effective technologies are developed for simultaneous removal of Sb, As and Pb from low-pH environments, which are often associated with oxidation of sulfidic ores and associated metal(loid) mobilization.

Various methods have been reported for the removal of Sb, As, and Pb from waters, such as chemical co-precipitation, membrane filtration, electrodialysis, coagulation/flocculation, ion-exchange, and adsorption [10-14]. Among these, adsorption has a number of advantages, such as easy operation, low costs and minimal sludge production [3]. However, some adsorbents have a limited adsorption capacity and/or slow adsorption kinetics. Adsorption processes might also require additions of metal ions or other chemical compounds, and the generation of adsorbents often requires a high-energy input. All the above leads to increased process costs and environmental impacts. Additional challenges can arise during the upscaling of contaminant removal processes into large-scale operations, and these should be considered also during the development and implementation of adsorption applications.

Al/Si-rich solid wastes are generated by industries in large amounts. Due to their large surface area, variable surface chemistry and high adsorption capacity [15], these industrial wastes attract increasing research interest for their potential to serve as cost-effective adsorbents in contaminant removal. Red mud (RM), a waste material generated during alumina production, typically comprises primarily Al, Si, Fe, and Ca oxides [16,17]. The global reserve of RM exceeds 4 billion tons, with an annual accumulation rate of 175.5 million tons [18]. RM is expected to effectively remove As, considering the high affinity of Al and Fe oxides to heavy metals as well as the alkaline nature (usual $\text{pH} > 10$) of RM [19], but no reports are available that would investigate Sb removal from aqueous solutions using red mud modified with wastewater. Adsorption of Pb using modified RM has been reported, but with a very limited removal capacity under acidic conditions ($\text{pH} < 3$) [20, 21]. A direct modification of alkaline RM using acidic Fe(III)-rich wastewater could be advantageous in sustainable large-

scale metal(loid) removal, thanks to a simplified adsorbent synthesis and reduced treatment costs.

Acid mine drainage (AMD) is low-pH mine effluents generated via oxidation of metal sulfides such as pyrite (FeS_2), with a great potential to contaminate the surrounding environment with acid and hazardous metal(loid)s. However, AMD can also be considered a secondary source of valuable metals and a cheap alternative to exogenous catalysts, due to elevated concentrations of dissolved Fe, Al, Cu, and Mn [22]. Previous studies have demonstrated that AMD may serve as a source of Fenton reagents (e.g., Fe and Mn) and Lewis acid catalysts, eliminating the costs on metal salts additions [23,24]. Chen et al. [25] reported that Fe(III) in AMD promoted arsenopyrite dissolution, and an addition of RM to Fe(III)- and As-rich acidic wastewater enhanced the rate of As(III) immobilization, indicating that AMD has the catalytic potential to drive RM transformations and modifications. To our best knowledge, no other study has reported the synthesis and use of RM adsorbents modified by AMD for Sb, As, and Pb removal under acidic conditions, and no experimental data describing such synthesis and adsorption mechanisms have been published.

In this work, simultaneous removal of Sb, As, and Pb was investigated using novel low-cost Fe/S/Ca/Al/Si-bearing adsorbents synthesized from RM modified with AMD. The transformations of RM and AMD solution chemistry were studied, monitoring the changes in AMD parameters and determining Sb/As/Pb adsorption characteristics of the precipitates generated under different solid (RM) to liquid (AMD) ratios ($S_{\text{RM}}/L_{\text{AMD}}$). In addition, metal(loid) removal mechanisms were evaluated by integrating aqueous- and solid-phase analyses. The findings obtained in this study could inform and assist the development of cost-effective methods for the treatment of acidic waters contaminated with Sb, As and/or Pb, using industrial wastes. The presented approach portrays a novel and sustainable strategy in resource utilization of RM and AMD.

2. Materials and methods

2.1. Materials

RM used in the experiments was obtained from an alumina processing plant in the Henan province, China. The elemental composition of RM analyzed by X-ray fluorescence spectroscopy (XRF; Axios mAX, Netherlands) was as follows (in wt.%):

38.86 O, 13.03 Al, 11.55 Ca, 11.52 Fe, 10.79 Si, 7.31 Na, 3.11 Ti, 2.26 K, 0.50 Mg, 0.48 S, and 0.59 others. The phase composition of the original RM, characterized by X-ray diffraction (XRD; D8 Advance, Bruker, Germany), was primarily cancrinite [$\text{Na}_6(\text{Al}_6\text{Si}_6\text{O}_{24})(\text{CaCO}_3)\cdot 2\text{H}_2\text{O}$], katoite [$\text{Ca}_3\text{Al}_2(\text{SiO}_4)(\text{OH})_8$], hematite [Fe_2O_3], calcite [CaCO_3], gibbsite [$\text{Al}(\text{OH})_3$], kaolinite [$\text{Al}_2\text{Si}_2\text{O}_5(\text{OH})_4$], perovskite [CaTiO_3], and muscovite [$\text{KAl}_2\text{Si}_3\text{AlO}_{10}(\text{OH})_2$], with minor amounts of diaspore [$\beta\text{-AlO}(\text{OH})$] and quartz [SiO_2]. The pH of the intact RM was 10.92. AMD used in this work was collected from the Dabaoshan Mine ($24^\circ 34' 28''\text{N}$, $113^\circ 43' 42''$), which is one of the largest polymetallic mines in South China [26]. The major elements in AMD, analyzed by inductively coupled plasma-optical emission spectrometry (ICP-OES; SPECTRO BLUE SOP, Spike Analytical Instruments, Germany), comprised (in mg/L): 695.3 Fe, 391.2 Al, 367.2 Ca, 222.3 Zn, 111.5 Mn, 54.6 Na, 39.98 Cu, 39.7 Si, 23.3 K, 1.6 Pb, 1.0 As, and 0.8 Sb. The pH and oxidation reduction potential (ORP) of the collected AMD were 2.06 and +572 mV, respectively.

2.2. Preparation of RM-based materials

RM was dried for 24 hours in an oven at 90°C , then passed through a 400-mesh sieve. The RM-based adsorbent was synthesized in 250 mL Erlenmeyer flasks containing 100 mL of filtered ($0.22\ \mu\text{m}$) AMD. To determine the effect of the $S_{\text{RM}}/L_{\text{AMD}}$ (w/v) ratio on the structure and composition of the materials, the synthesis was conducted by the addition of 0.2, 0.4, 0.6, 0.8, and 1.0 g RM (giving the final $S_{\text{RM}}/L_{\text{AMD}}$ ratios (in g/L) of 2:1, 4:1, 6:1, 8:1, and 10:1). The flasks were incubated at 30°C and 170 rpm. After 96 hours of incubation, the precipitates were harvested, washed three times with deionized water (DIW), dried in vacuum, and finally characterized and used in the below described experiments.

2.3. As and Sb adsorption experiments

In the adsorption experiments, the following aqueous stock solutions (1000 mg/L) were used: As(III) (as NaAsO_2 in DIW), As(V) ($\text{Na}_2\text{HAsO}_4\cdot 7\text{H}_2\text{O}$), Sb(III) ($\text{C}_4\text{H}_4\text{KO}_7\text{Sb}\cdot 0.5\text{H}_2\text{O}$), and Sb(V) ($\text{KSb}(\text{OH})_6$). The adsorption tests were performed in 100-mL Erlenmeyer flasks containing 1 g/L adsorbent and 50 mL of the As(III/V) or Sb(III/V) solutions, with final concentrations of 200 mg/L for As(III/V), and 200 and 1000 mg/L for Sb(III/V). Adsorption isotherms were determined at metal(loid) concentrations ranging from 0 to 160 mg/L for As(III), As(V), and Sb(III), and from 0

to 1,280 mg/L for Sb(V). The effects of the presence of co-existing anions (i.e., CO_3^{2-} , SO_4^{2-} , PO_4^{3-} , and NO_3^-) and their concentration (from 0 to 60 mg/L) on As(III/V) and Sb(III/V) removal were also investigated. In all above experiments, the initial solution pH was adjusted to 2.0 ± 0.05 (using H_2SO_4), and 0.01 M NaNO_3 was used as a background electrolyte. The flasks were incubated for 48 hours at 30 °C and 170 rpm. Liquid samples (0.5 mL) were regularly collected, filtered (0.22 μm), and analyzed for As and Sb concentrations.

2.4. Pb removal procedure

A Pb(II) stock solution of 1 g/L was prepared by dissolving $\text{Pb}(\text{NO}_3)_2$ in DIW. Experiments on Pb removal were performed in a 100 mL flask containing 50 mL of Pb(II) solution (with initial Pb(II) concentrations from 0 to 1,000 mg/L) and 1 g/L adsorbent materials formed under different $S_{\text{RM}}/L_{\text{AMD}}$ ratios. To investigate the effect of pH (over the range from 2 to 7) on the rate of Pb removal, adsorbents (1 g/L) were incubated for 48 hours with 1,000 mg/L Pb(II). The effects of different concentrations (from 0 to 60 mg/L) of other metal cations (i.e., Cu^{2+} , Zn^{2+} , Al^{3+} , and Mn^{2+}) on Pb(II) removal were also investigated. The initial pH of Pb solutions was adjusted using 1 M HNO_3 or NaOH , and 0.01 M NaNO_3 was used as a background electrolyte.

2.5. Adsorbent regeneration

To assess the regeneration potential of the RM-based adsorbents, an experiment consisting of four adsorption-desorption cycles was performed. Adsorption was carried out with 1 g/L adsorbent in 50 mL of As(III/V), Sb(III/V) or Pb(II) solutions (all 100 mg/L; pH of 2.0 ± 0.05). After 48 hours incubation at 30 °C, the adsorbents were collected by filtration and the concentration of residual metal(loid)s was determined. For the determination of desorption, metal(loid)s-bearing adsorbents were added into 100 mL of 0.5 M NaOH solution, and after 6 hours of stirring (at 170 rpm), the adsorbents were collected, washed, dried and used in another sorption cycle.

2.6. Analytical methods

The concentrations of dissolved As(III/V) and Sb(III/V) were determined in liquid samples using high-performance liquid chromatography combined with inductively coupled plasma-mass spectrometry (HPLC-ICP-MS; 7700x, Agilent Technologies, USA), with an anion exchange column. Other soluble elements were analyzed using ICP-OES.

The surface morphology and structure of solid samples were characterized by a field-emission scanning electron microscope (FE-SEM; TESCAN MIRA3, Czech Republic) equipped with an energy dispersive spectrophotometry (EDS). X-ray diffraction (XRD) patterns were determined using a powder XRD with Cu K radiation ($\lambda = 0.154$ nm). The BET (Brunauer–Emmett–Teller) specific surface area, pore size, and pore volume of the adsorbents were analyzed using the ASAP-2460 instrument (Micromeritics, USA). The Fourier-transform infrared spectrometry (FT-IR) analysis was conducted on a Nicolet iS50 spectrometer (Thermo Fisher Scientific, USA), with the KBr pressed disk technique. The transformation of the binding energy and valence states of solid samples were analyzed using X-ray photoelectron spectroscopy (XPS) (K-Alpha, Thermo Fisher Scientific, USA), with Al K α radiation (1,486.6 eV) and all binding energies standardized to the C1s peak at 284.8 eV. The microstructure of the solids as well as the element distribution on their surface were analyzed using a transmission electron microscope (TEM; Tecnai G2 F20 S-TWIN, FEI, USA).

The arsenic speciation in solid samples were investigated by X-ray absorption spectroscopy (XAS), including X-ray absorption near edge structure (XANES) and extended X-ray absorption fine structure (EXAFS) spectroscopy, on beamline 1W2B (in a fluorescence mode) at the Beijing Synchrotron Radiation Facility (BSRF; Beijing, China), with a Si (111) double-crystal monochromator. The electron storage ring was operated at 2.5 GeV with a maximum current of 250 mA. The obtained data were analyzed using Athena and Artemis software from the IFEFFIT package [27, 28]. EXAFS data were extracted from raw spectra and the edge energy value (E_0) was chosen at the edge inflection point for all samples. The radial distribution functions (RDFs) were obtained from the $k^3\chi(k)$ oscillation by Fourier Transform (FT). The distinct RDF shells were then inversely transformed for spectral simulation by a curve-fitting method. The crystal information files of As₂O₃, As₂O₅, FeAsO₄·2H₂O, and AlAsO₄ from the American Mineralogist Crystal Structure Database were used to calculate the theoretical models fitted to individual RDFs obtained from the EXAFS data.

3. Results and discussion

3.1. Adsorbent characterization

3.1.1. Morphology and phases characterized by SEM and XRD

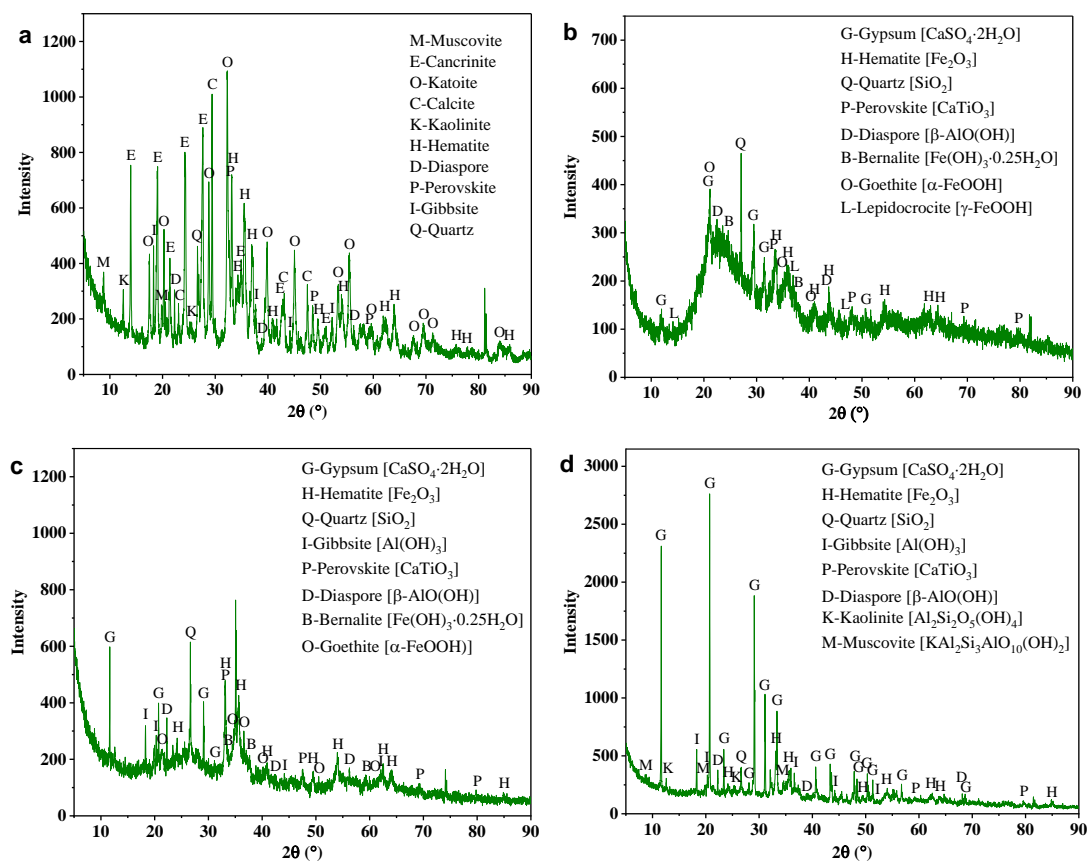
Original RM was an irregularly shaped mass containing sheet-like structures (Fig. 1a). After 96 hours reaction with AMD under S_{RM}/L_{AMD} of 2:1, the precipitate was in the form of flat amorphous aggregates with a large number of nanoparticles (~20 nm diameter) attached on the surface (Fig. 1b). With S_{RM}/L_{AMD} increasing to 4:1, the morphology of the precipitate changed into poorly crystallized, spherical microstructures with a diameter of approximately 200 nm (Fig. 1c). These nanoparticles grew more regular and uniform, showing smoother surfaces, when S_{RM}/L_{AMD} increased further ($\geq 6:1$), indicating improved crystallization of the spherical nanoparticles under higher S_{RM}/L_{AMD} (Fig. 1d-f). Additionally, long flake-like structures corresponding to gypsum ($\text{CaSO}_4 \cdot 2\text{H}_2\text{O}$) [29] were observed in the latter precipitate (Fig. 1d-f). Fe^{3+} and H^+ in AMD acted as key agents in the transformation of RM, and the S_{RM}/L_{AMD} , which directly affected solution pH and the degree of RM dissolution, determined the surface structure of the precipitate (Fig. 1g).



Fig. 1. SEM images of (a) original RM, and precipitated adsorbents synthesized under

S_{RM}/L_{AMD} ratio of (b) 2:1, (c) 4:1, (d) 6:1, (e) 8:1, and (f) 10:1; (g) Schematic diagram of the formation of adsorbents synthesized from RM under the catalysis by AMD.

The results of an XRD analysis of the phase composition of the adsorbents (Fig. 2) showed that after reaction with AMD under S_{RM}/L_{AMD} of 2:1 (for 96 hours), most of the original RM peaks disappeared, except for those of hematite, perovskite, diaspore, and quartz, all of which seemed relatively stable under acidic conditions [30]. Meanwhile, new phases were detected, such as gypsum [$CaSO_4 \cdot 2H_2O$], bernalite [$Fe(OH)_3 \cdot 0.25H_2O$], goethite [$\alpha-FeOOH$], and lepidocrocite [$\gamma-FeOOH$] (Fig. 2b). Dissolution of alkaline RM results in the release of hydroxyl groups into AMD, which favors precipitation of Fe(III) as $Fe(OH)_3$ (Eq. (1)). It has been postulated that the solid phase formed depends on pH and SO_4^{2-} concentration in AMD [31]. For instance, goethite is an Fe(III) phase stable at a wide range of pH, and often plays an important role in controlling the fate of toxic metal(loid)s in AMD, due to its high specific surface area and adsorption capacity [32]. In contrast, lepidocrocite is much less common than goethite, and its precipitation is favored by the presence of low molecular weight Fe(III) species and inhibited by low pH values and high concentrations of SO_4^{2-} [33].



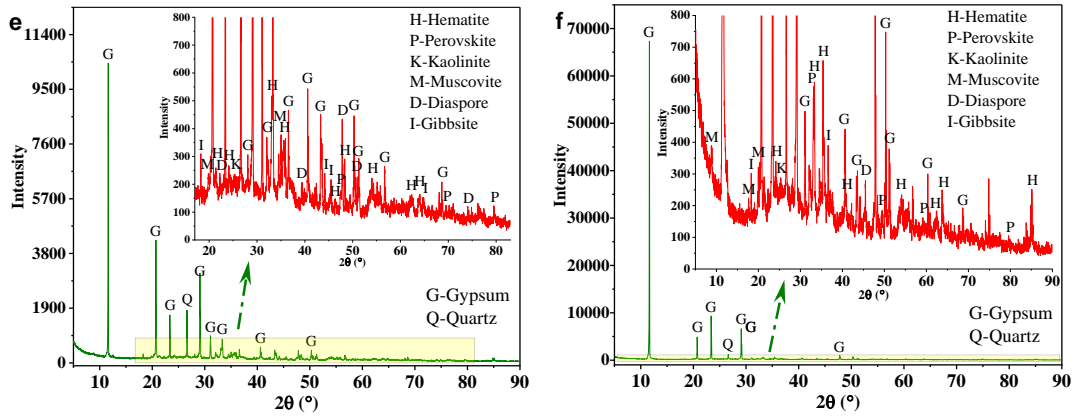
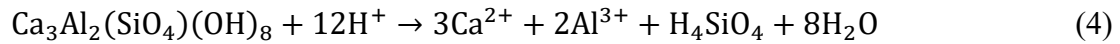


Fig. 2. XRD patterns of (a) original RM, and precipitated adsorbents synthesized under S_{RM}/L_{AMD} ratio of (b) 2:1, (c) 4:1, (d) 6:1, (e) 8:1, and (f) 10:1.

In the XRD spectrum of the adsorbent formed under S_{RM}/L_{AMD} of 4:1, the intensity of the peaks for gypsum, hematite, diaspore, and gibbsite increased, while the peak intensities for goethite and lepidocrocite decreased (Fig. 2c), compared to the XRD spectrum of the adsorbent formed under S_{RM}/L_{AMD} of 2:1. Since the concentration of SO_4^{2-} in AMD is generally high (> 3 g/L), the formation of gypsum (Eq. (2)) during the adsorbent synthesis depends on the concentration of Ca^{2+} released from RM (Eqs. (3,4)). It is worth noting that the release of Ca^{2+} is affected by the fact that the increase in pH caused by an addition of alkaline RM inhibits dissolution of aluminosilicates. When $S_{RM}/L_{AMD} \geq 6:1$, the gypsum peaks were dominant in the adsorbent spectrum, followed by kaolinite, diaspore, hematite, and muscovite peaks (that are characteristic for RM phases), while goethite and lepidocrocite peaks were not detected (Figs. 2d-f).



3.1.2. BET adsorption analysis

The N_2 adsorption-desorption isotherms together with the pore size distribution of RM-based adsorbents are shown in Fig. S1 and Table S1, respectively. All adsorbents (i.e., those formed under different S_{RM}/L_{AMD} ratios, as well as original RM) were characterized by type-IV hysteresis loops, confirming the existence of a mesoporous structure [34]. The surface area (S_{BET}) of the precipitates increased with an increasing S_{RM}/L_{AMD} ratio, yielding 151.0, 172.1, and 188.4 m^2/g in the assays with S_{RM}/L_{AMD} of

2:1, 4:1, and 6:1 respectively, with all values being significantly higher than S_{BET} of the original RM. With further increase of S_{RM}/L_{AMD} to 8:1 and 10:1, the S_{BET} decreased. The pore volume of the precipitates also increased with an increasing S_{RM}/L_{AMD} ratio (Table S1). It has been previously reported that a larger pore volume, as well as a mesoporous nature of an adsorbent material, may result in an increased number of active sites for Sb and/or As adsorption [35].

3.1.3. Changes in solution parameters during adsorbent synthesis

Changes in the concentration of soluble elements were monitored during the synthesis of the RM-based adsorbents under different S_{RM}/L_{AMD} ratios. Fig. 3a shows that the addition of RM resulted in a decrease in the concentration of dissolved Fe in AMD, with the Fe removal rate rising with increasing S_{RM}/L_{AMD} ratio, reaching 56.52, 99.67, 99.76, and 99.83% in the assays with S_{RM}/L_{AMD} of 2:1, 4:1, 6:1, and 8:1, respectively. The dissolution of alkaline RM in AMD also led to a sharp increase in pH (Fig. S2a) and decrease in ORP values (Fig. S2b), and the dissolution of RM resulted in a release of Al, Si, Ca, K, and Na into solution (Fig. 3b-f). The precipitation of Fe(III) generates H^+ (Eq. (1)), which resulted in a slight decrease in pH detected after day 1 (Fig. S2a). The concentrations of soluble Al, Si, and Ca exhibited maximum values of 580.9, 241.7, and 606.7 mg/L, respectively, in the assay with S_{RM}/L_{AMD} ratio of 4:1.

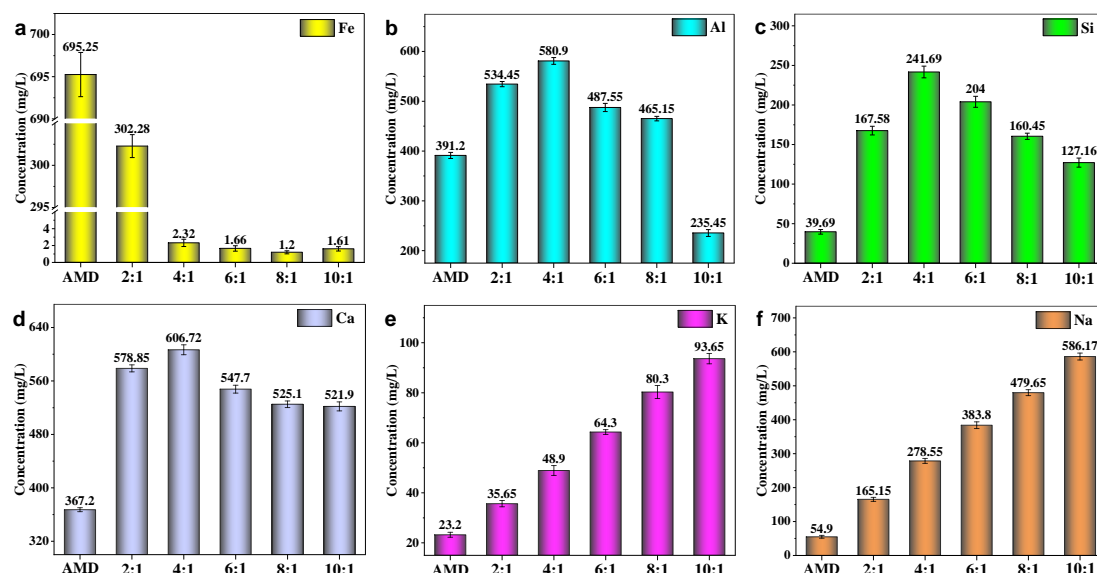


Fig. 3. Concentrations of soluble (a) Fe, (b) Al, (c) Si, (d) Ca, (e) K, and (f) Na in AMD and in liquid samples after the synthesis of different adsorbents (under S_{RM}/L_{AMD} of 2:1, 4:1, 6:1, 8:1, and 10:1).

3.2. Adsorption of As and Sb onto RM-based adsorbents

3.2.1. As(III/V) and Sb(III/V) removal capacities

Fig. S3 shows that RM-based adsorbents formed under S_{RM}/L_{AMD} ratios of 2:1 (RA2), 4:1 (RA4), 6:1 (RA6), 8:1 (RA8), and 10:1 (RA10) removed 69.0, 81.2, 67.5, 59.7, and 40.2% of As(V) in 48 hours, respectively (all at pH 2.0). These were significantly higher values than the As(V) removal capacity of the original RM material (accounting for 15.2%). Similarly to As(V), the highest removal of As(III) (12.8%) among the tested adsorbents was achieved with RA4. By comparison, the materials showed an excellent removal capacity for Sb(V), reaching 70.1, 99.3, 98.5, 97.1, 97.7, and 94.0% using original RM, RA2, RA4, RA6, RA8 and RA10, respectively. These values were significantly higher than the removal capacities for Sb(III) (which reached 17.2, 58.8, 57.3, 38.6, 31.8, and 22.9% respectively), under similar conditions. The above results indicate that RA4 is the most efficient adsorbent for As(III/V) adsorption, while RA2 is the most suitable for Sb(III/V) removal.

3.2.2. Adsorption kinetics and isotherms

Based on the above results, RA4 and RA2 were used to investigate adsorption kinetics and isotherms for As and Sb, respectively. The time-dependent adsorption behavior of As(III/V) (Fig. 4a) and Sb(III/V) (Fig. 4b) showed high adsorption rates within 3 hours, due to the high As and Sb concentrations and sufficient numbers of adsorption sites. With elapsing time, most of the adsorption sites became saturated, which resulted in a decrease in the adsorption rates, until equilibrium was reached. To investigate further the adsorption of As(III/V) and Sb(III/V), the kinetic data were fitted using pseudo-first-order and pseudo-second-order models (described in detail in Supplementary Materials (SM)). Both non-linear (Fig. 4a, b and Table S2) and linear (Fig. S4) fitting results show that the pseudo-second-order model was more suitable to the description of the As(III/V) and Sb(III/V) adsorption processes, indicating that chemical interactions occurred between the As/Sb species and adsorbents [36].

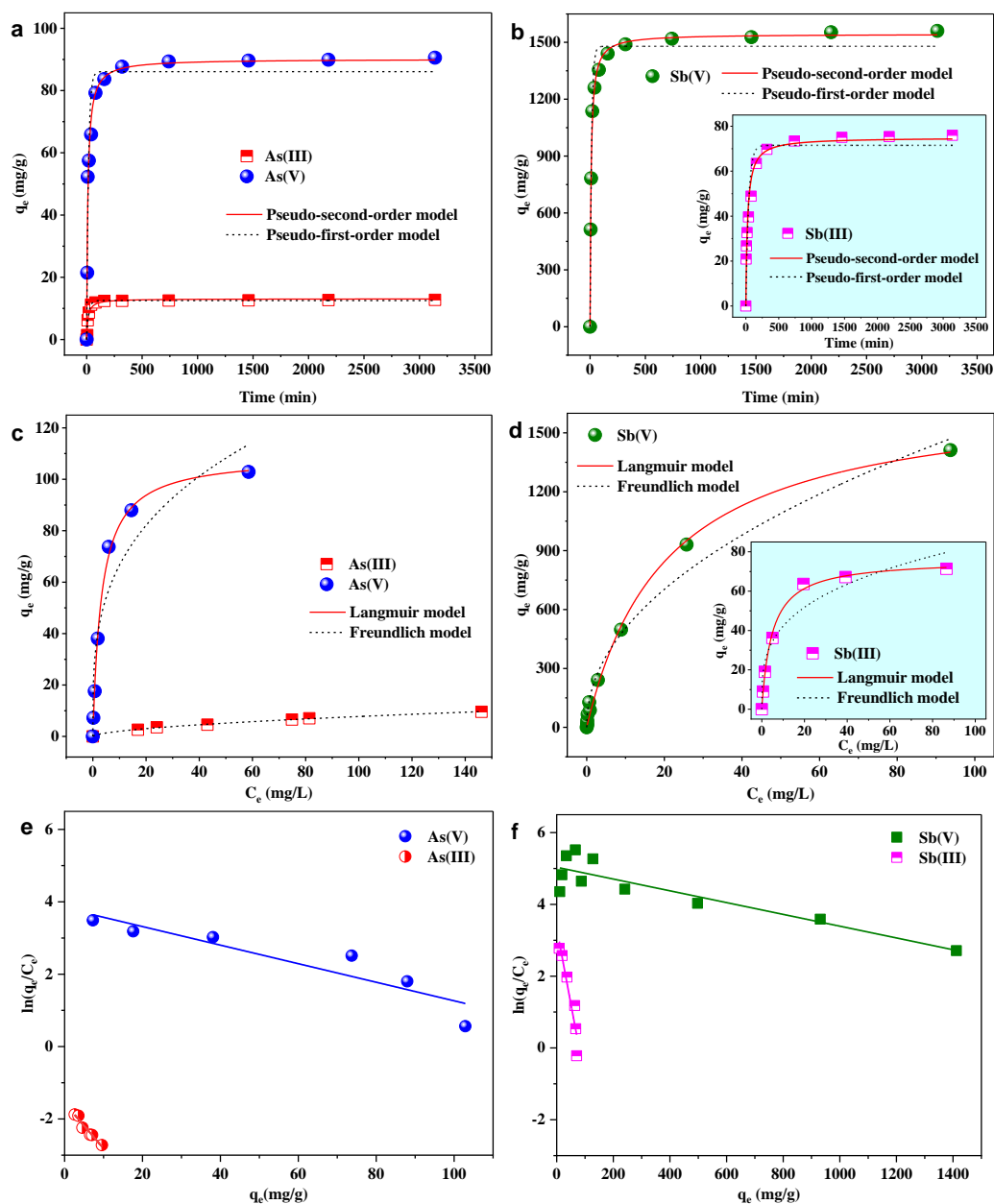


Fig. 4. (a, b) Adsorption kinetics and (c, d) isotherms for the adsorption of: (a, c) As(III/V) onto the adsorbent formed under S_{RM}/L_{AMD} ratio of 4:1 (RA4), and (b, d) Sb(III/V) onto the adsorbent formed under S_{RM}/L_{AMD} ratio of 2:1 (RA2); Plots of $\ln(q_e/C_e)$ vs. q_e for adsorption of (e) As(III/V) onto RA4, and (f) Sb(III/V) onto RA2. Legend: q_e = equilibrium sorption capacity of adsorbents, C_e = equilibrium concentration of metalloids.

Adsorption isotherms were constructed to evaluate the adsorption capabilities of the RA4 and RA2 adsorbents, and to describe in more detail the metalloid-adsorbent interactions involved. The Langmuir and Freundlich isotherm models (shown in SM)

were applied to the isotherm data. The fitting results (Fig. 4c, d and Table S3) showed that out of the two models the Langmuir model was more suitable to describe adsorption of As(V), Sb(III), and Sb(V), indicating that the adsorption processes of these three species were homogeneous and the adsorption sites on RA4 and RA2 were filled by the metalloids in a monolayer [37]. However, unlike that of As(V) and Sb(III/V), the adsorption of As(III) followed the Freundlich model, indicating this process occurred in multiple layers [38]. The above findings were also supported by the linear fitting results shown in Fig. S5.

The maximum Sb(V) adsorption capacity (q_m) of RA2 was 1,637.8 mg/g, based on the fitting results (Table S3). This value was more than 20 times greater than that for Sb(III) adsorption (which reached 80.2 mg/g). The q_m of RA4 for As(V) and As(III) adsorption was 109.2 and 16.4 mg/g, respectively. In comparison to published data, the RM-based adsorbents formed under S_{RM}/L_{AMD} of 2:1 and 4:1 demonstrated superior adsorption capacities for Sb(III/V) and As(III/V), respectively, outperforming many of the adsorbents described previously (Table S4).

As shown in Figs. 4e and f, The negative ΔG^0 values obtained for the As(V)-RA4 (-9.93 kJ/mol), Sb(III)-RA2 (-8.42 kJ/mol), and Sb(V)-RA2 (-12.68 kJ/mol) systems indicated that these adsorption processes were spontaneous reactions [39], proving the feasibility of the use of the RM-based adsorbents for removal of the above metalloids. Moreover, the results are consistent with ΔG^0 for adsorption of Sb(III/V) onto FeMn binary oxides prepared from an Mn encapsulated carboxymethyl cellulose-Fe(III) hydrogel (which ranged between -1.54 and -3.03 kJ/mol in the temperature range of 25-35 °C) [40]. The positive ΔG^0 (3.93 kJ/mol) for As(III) removal by RA4 indicated that the adsorption process was not spontaneous at the temperature of 30 °C. All parameters related to the above are shown in Table S5.

Fig. S6 shows the presence of SO_4^{2-} and NO_3^- had little effect on the removal of As(III/V) and Sb(III/V) in the tested concentration range, while PO_4^{3-} , as well as CO_3^{2-} , caused an evident decrease in the removal efficiencies of As(III/V) and Sb(III/V). This lowered removal rate was evident particularly for As(V) and Sb(V), likely due to the chemical similarity of the anions. The results indicate that the RM-based adsorbents synthesized in this study are particularly suitable for the removal of metalloids from SO_4^{2-} rich wastewater such as AMD and nonferrous smelting wastewaters.

3.3. Metalloid adsorption mechanisms

3.3.1. Arsenic adsorption on RA4

Fig. S7 shows the morphology of the adsorbents from both As(V) and As(III) assays composed of small spherical microstructures, showing an overall structure similar to that of RA4 before As adsorption (Fig. 1c). Based on EDS results, higher contents of As (19.56%), Al (2.63%), Ca (1.3%), and Fe (37.92%) were distributed on the surface of the adsorbent in the As(V) assay, compared to those in the As(III) assay (7.21 As, 2.04 Al, 0.23 Ca, and 31.85% Fe). The ability of Al(III) and Fe(III) to promote As(V) immobilization via the formation of Al(III)-and/or Fe(III) (hydr)oxides has been reported previously [41,42].

Most of the solid phases detected in the adsorbent before As adsorption (e.g., $\text{CaSO}_4 \cdot 2\text{H}_2\text{O}$, Fe_2O_3 , $\text{Al}(\text{OH})_3$, CaTiO_3 , $\beta\text{-AlO}(\text{OH})$, $\text{Al}_2\text{Si}_2\text{O}_5(\text{OH})_4$, and $\text{KAl}_2\text{Si}_3\text{AlO}_{10}(\text{OH})_2$) were detected also after As(V) adsorption (Fig. S8a). Unlike in the FT-IR spectra for the RA4 adsorbent after As(III) adsorption (exhibits an As(III)–O vibration at 808 cm^{-1}), a strong band assigned to As(V)–O–Fe stretching vibration of ferric arsenate (at 825 cm^{-1}) was detected in the precipitate after As(V) adsorption (Fig. S8b) [43]. The intensities of the bands for –OH (at $3,392\text{ cm}^{-1}$), Fe–OH ($1,125\text{ cm}^{-1}$), and Al–O–Si (at 685 cm^{-1}) decreased after As(III), and even more after As(V), adsorption (Fig. S8b). This can be ascribed to the dissolution of minor amounts of aluminosilicates (such as $\text{Al}_2\text{Si}_2\text{O}_5(\text{OH})_4$; Eq. (5)) under acidic conditions, which can promote the formation of a silica-based shell on the surface of Fe-As precipitates, thus enhancing the stability of the As-bearing precipitate.



Fig. 5a shows that after reaction with As(V), the intensities of the peaks corresponding to Fe 2p, O 1s, Si 2p, and As 3d were higher than the peak intensities after As(III) adsorption, showing that As was adsorbed in both cases, but the adsorption of As(V) was significantly higher than that of As(III) (Fig. 5b). While no other As species were detected after reaction with As(V) (Fig. 5c), the As 3d line could be fitted with 87.1% As(III) (44.3 eV) and 12.9% As(V) (45.2 eV) after reaction with As(III)

(Fig. 5d), indicating that partial oxidation of As occurred either during the As(III) adsorption process or under the X-ray beam.

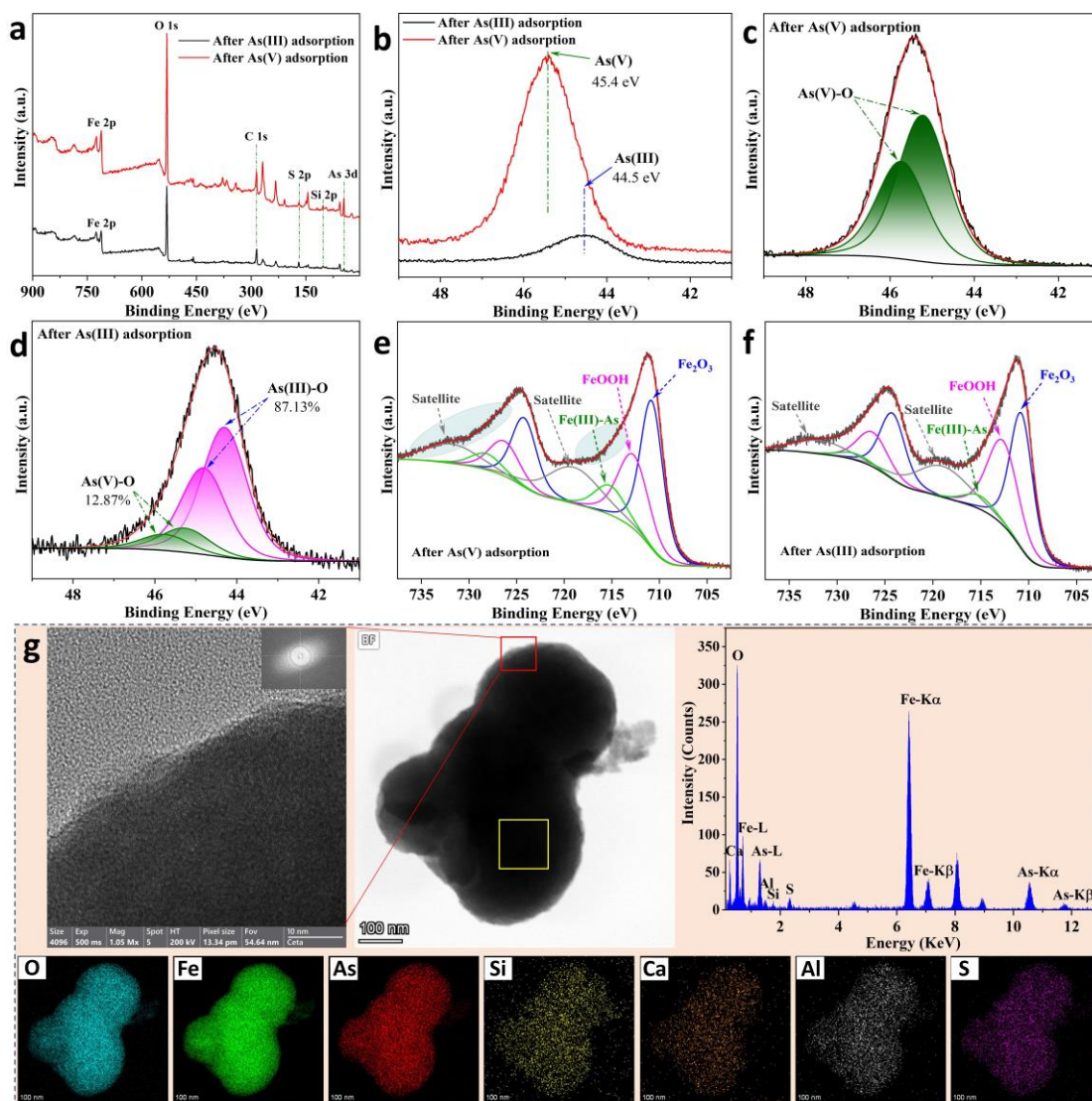
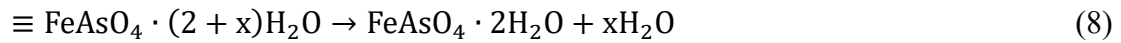
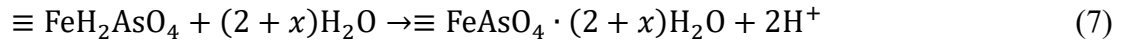
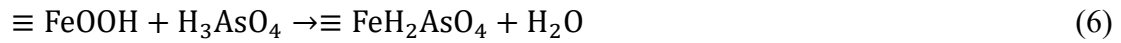


Fig. 5. XPS spectra of the RA4 adsorbent after As(V) adsorption. (a) XPS full scan spectra; (b) As 3d_(5/2) high resolution scan; XPS spectra of surface (c, d) As and (e, f) Fe species in the RA4 adsorbent after (c, e) As(V) and (d, f) As(III) adsorption; (g) TEM-EDS and elemental mapping of the RA4 adsorbent after As(V) adsorption.

As presented in Figs. 5e and f, the XPS spectra of Fe 2p could be fitted with three components corresponding to Fe₂O₃ (710.8 and 724.2 eV), FeOOH (712.7 and 726.3 eV), and Fe(III)-As (715.2 and 728.2 eV), next to the satellite peaks (at 719.0 and 731.8 eV) [44,45]. The proportion of FeOOH (25.3%) on the surface of RA4 was significantly

lower and the proportion of Fe(III)-As (11.0%) (which may be attributed to scorodite [46]) was much higher after reaction with As(V) than after reaction with As(III) (37.6 versus 3.08% respectively) (Table S6). These changes indicate that surface complexation reactions occurred between Fe(III) species and As(V/III). It has been previously described that at low pH (< 3.0), FeOOH is unstable, and AsO_4^{3-} can react with Fe(III) after replacing the hydroxyl group to form poorly crystalline ferric arsenate or scorodite in three steps (Eqs. (6-8)) [47]. The results of TEM analysis (Fig. 5g) show that the surface of RA4 comprised an amorphous layer after As(V) adsorption, and the high contents of Fe and O with similar element distribution shapes to that of As further indicate that $\equiv \text{Fe} - \text{OH}$ in RA4 played a major role in the As(V) adsorption processes.



XAS analysis was conducted to further clarify the mechanisms of As adsorption. The normalized As K-edge XANES spectrum of RA4 after As adsorption shows no apparent changes in the oxidation state of As(V) and As(III) during the adsorption processes (Fig. 6a). The k^3 -weighted $\chi(k)$ As EXAFS spectra for the As-adsorbed RA4 precipitates, and their Fourier transforms and shell fitting parameters are shown in Fig. 6(b, c) and Table S7, respectively. The first shells from As(V)-RA4 and As(III)-RA4 (fitted by 3.1 oxygen atoms at an As-O distances of 1.69 and 1.78 Å; Table S7) corresponded closely to As(V)-O and As(III)-O distances, respectively (Fig. 6c). These findings are consistent with previously reported values for As-adsorbed Fe (oxyhydr)oxides [48, 49]. In the As(V)-RA4 system, an As-Fe peak at distance near 2.8 Å in the EXAFS spectrum indicated the presence of bidentate-mononuclear (2E) complexes [50]. Meanwhile, an As-Al distance at near 3.2 Å implied that Al in RA4 also contributed to As(V) adsorption, which is in agreement with findings of a previous study investigating adsorption of As onto Al hydroxide [51]. For the As(III)-RA4 system, As-Fe distances of 2.9 and 3.4 Å were assigned to bidentate-mononuclear (2E) and bidentate binuclear corner-sharing (2C) surface complexes, respectively [49].

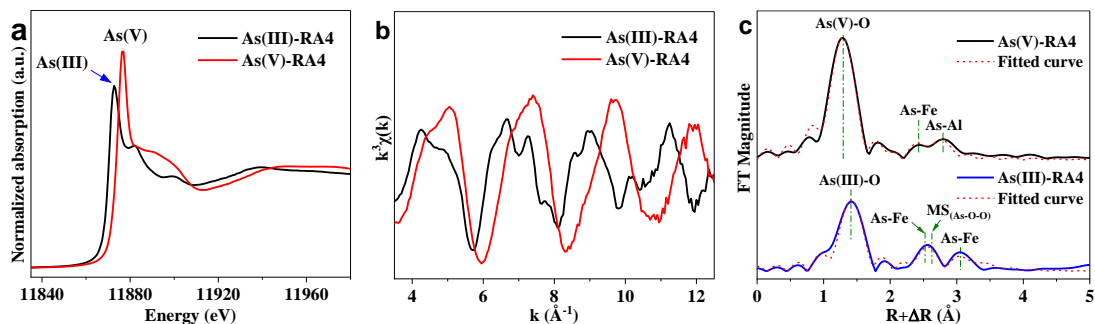


Fig. 6. (a) K-edge XANES spectra of RA4 adsorbent after As(V) and As(III) adsorption; (b) k^3 -weighted $\chi(k)$ data; (c) magnitude of the Fourier-transformed As K-edge EXAFS data for RA4 after As(V) and As(III) adsorption.

3.3.2. Antimony adsorption on RA2

The amorphous spherical nanoparticles (~ 100 nm diameter; composing mainly of O, Sb, Fe, and Ca; Fig. 7a) formed on the surface of the adsorbent after Sb(V) adsorption differed from those on RA2 before Sb adsorption (Fig. 1b), while no structural changes were observed in the adsorbent after Sb(III) adsorption (Fig. 7b). The highly similar mapping images of Sb, Ca, and O indicated that Ca may have played an important role in Sb(V) immobilization. Adding Ca^{2+} to control precipitation of Ca-Sb oxides and/or oxyhydroxides has previously been postulated to be an effective way for Sb removal from waters, with the precipitation processes being significantly affected by and dependent on pH [52]. Under acidic conditions, $[\text{Sb}(\text{OH})_6]^-$ is initially transformed to HSb_2O_6^- (Eq. (9)), which can then react with Ca^{2+} to form Ca antimonates such as $\text{CaSb}_2\text{O}_5(\text{OH})_2$ (Eq. (10)) [53]. The XRD results show that a large amount of $\text{CaSb}_2\text{O}_5(\text{OH})_2$ (identified using the JCPDS card 32-0154) was formed on the adsorbent surface after Sb(V) adsorption, while gypsum and several Fe(III) hydroxy compounds (e.g., lepidocrocite) observed in intact RA2 were not detected after Sb(III) and Sb(V) adsorption (Fig. 7c).



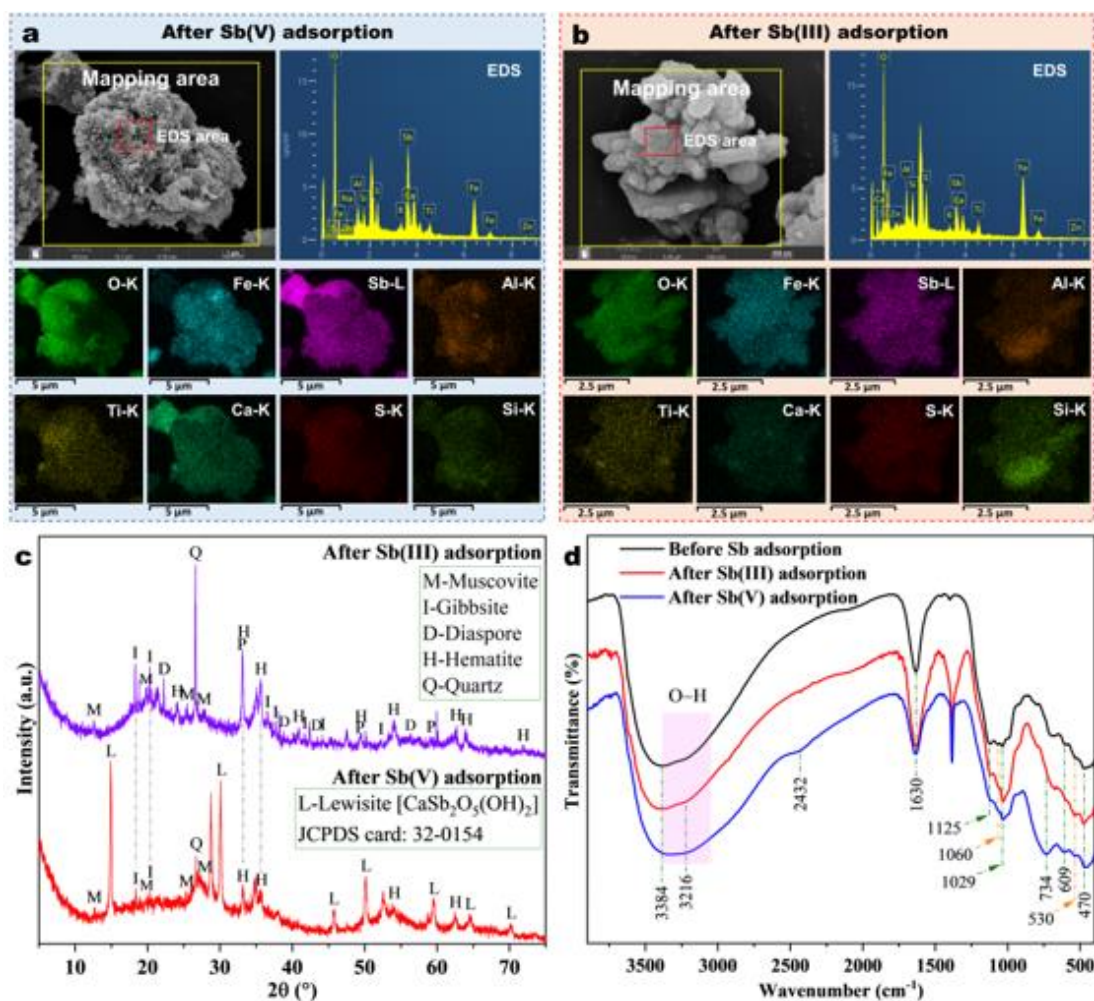


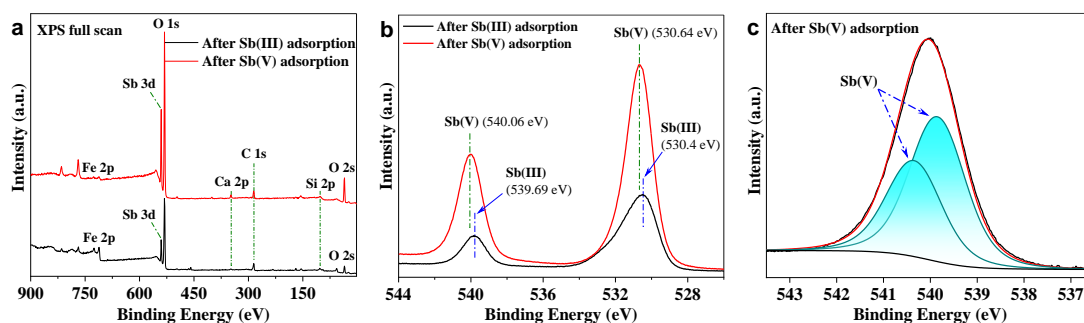
Fig. 7. SEM-EDS images and elemental mapping of the RA2 adsorbent (formed under S_{RM}/L_{AMD} of 2:1) after (a) Sb(V) and (b) Sb(III) adsorption; (c) XRD pattern of the precipitate after Sb(III/V) adsorption; (d) FT-IR spectra of the adsorbent before and after Sb(III/V) adsorption.

The surface chemistry characterizations by FT-IR (Fig. 7d) show that the intensity of the peak attributed to the H–O–H vibration of associated water molecules (at 1,630 cm^{-1}) increased after Sb(III) adsorption and decreased after Sb(V) adsorption on RA2, which may be ascribed to the effects of electrostatic complexation between Sb and RA2. Meanwhile, the intensity of the peak (at 3,384 cm^{-1}) corresponding to structural –OH groups decreased and shifted to a lower wavenumber after Sb(III/V) adsorption, indicating that –OH interacted with both Sb species. Upon Sb adsorption, the intensity of the peaks assigned to Fe–OH (1,125 and 1,060 cm^{-1}) noticeably decreased, while a band corresponding to Sb–O vibration newly appeared (at 734 cm^{-1}) [54]. The above results indicate that (similarly to Ca^{2+}) Fe-hydroxyl groups (i.e., $\equiv \text{Fe} - \text{OH}$) on the

surface of RA2 (which was formed via reactions between RM and Fe^{3+} in AMD) could adsorb large amounts of Sb (particularly Sb(V)) through chemical reactions. Under acidic conditions, $\equiv \text{Fe} - \text{OH}$ is protonated to $\equiv \text{Fe} - \text{OH}_2^+$, which can interact with the negatively charged $[\text{Sb}(\text{OH})_6]^-$ and form $[\equiv \text{Fe} - \text{OH}_2^+ \cdot \text{Sb}(\text{OH})_6^-]$ complexes, which are then transformed into a more stable chemical state ($\equiv \text{Fe} - \text{O} - \text{Sb}$) (Eq. (11)) [55].



The intensity of the peaks assigned to Sb 3d, O 1s, and Ca 2p in full-range XPS spectra of the RA2 adsorbent were significantly higher after adsorption of Sb(V) than after reaction with Sb(III) (Fig. 8a). The corresponding Sb 3d scan showed two peaks for each Sb species (540.06 and 530.64 eV for Sb(V); 539.69 and 530.4 eV for Sb(III); Fig. 8b) [56]. No reduction of Sb(V) was detected on the surface of RA2 during the Sb(V) adsorption process (Fig. 8c). In contrast, in the case of Sb(III) adsorption, the Sb 3d line could be fitted with 72.4% Sb(III) and 27.6% Sb(V) (Fig. 8d), indicating a certain level of Sb(III) oxidation by RA2 occurred, which is likely to have contributed to the high adsorption capacity for Sb(III) (80.2 mg/g; Fig. 4). The Fe peak intensity was lower after reaction with Sb(V) than after Sb(III) adsorption (Fig. 8a, e, f), further confirming that surface Fe species were involved in Sb(V) immobilization. The relative proportions of FeOOH and Fe_2O_3 were 35.45 and 40.27%, respectively, in the adsorbent after Sb(III) adsorption, while a lower content of FeOOH (29.2%; as well as a higher content of Fe_2O_3) was determined after reaction with Sb(V) (Table S8).



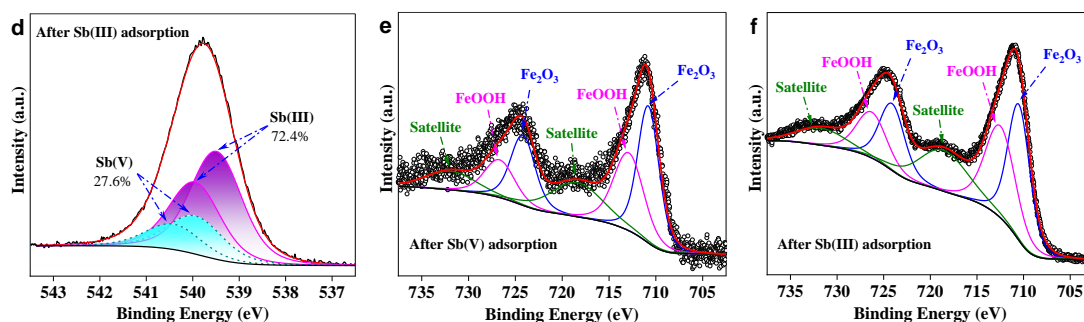


Fig. 8. XPS spectra of the RA2 adsorbent after Sb adsorption: (a) XPS full scan spectra; (b) Sb 3d_(3/2) high resolution scan; XPS spectra of surface (c, d) Sb and (e, f) Fe species in the adsorbent after (c, e) Sb(V) and (d, f) Sb(III) adsorption.

To describe the microstructure and composition of the RA2 adsorbent after Sb(V) adsorption, HRTEM imaging with elemental mapping and XPS were performed (Fig. 9). The spherical nanoparticles (SNPs) formed on the adsorbent surface after reaction with Sb(V) showed a core-shell structure with amorphous surfaces (Fig. 9a, b). The HRTEM analysis showed two types of clear lattice fringes with d-spacing values of 0.247 and 0.301 nm in the core, corresponding to the (110) plane of Fe₂O₃ and the (222) plane of CaSb₂O₅(OH)₂, respectively (Fig. 9a). The EDS mapping (Fig. 9c) showed similar distributions for Sb and Ca, further confirming that CaSb₂O₅(OH)₂ was the main component of the SNP core. Besides, based on the imaging, Fe surrounded the Ca/Sb-bearing core, and an Si-containing component was detected in the outermost layer.

The Si 2p XPS spectra indicated that speciation transformations of silicon occurred during the Sb(V) immobilization process, based on the broad peak shift (from 102.9 to 103.4 eV) after reaction with Sb(V), together with a decrease in its intensity (Fig. 9d) [57]. The silicon in RA2 before Sb(V) adsorption comprised mainly cancrinite [Na₆(Al₆Si₆O₂₄)(CaCO₃)·2H₂O, in RM], with small amounts of a silica gel formed via reactions between RM and AMD (Fig. 9e.) After reaction with Sb(V), the silica gel content increased (while the muscovite content decreased significantly) (Fig. 9f). Based on XRD, FT-IR, HRTEM, and XPS combined results, the structure and composition of the SNPs formed after Sb(V) immobilization are shown in Fig. 9g. It is expected that the silica gel layer coating the surface of the Sb-containing components enhances the stability of the Sb-bearing precipitate.

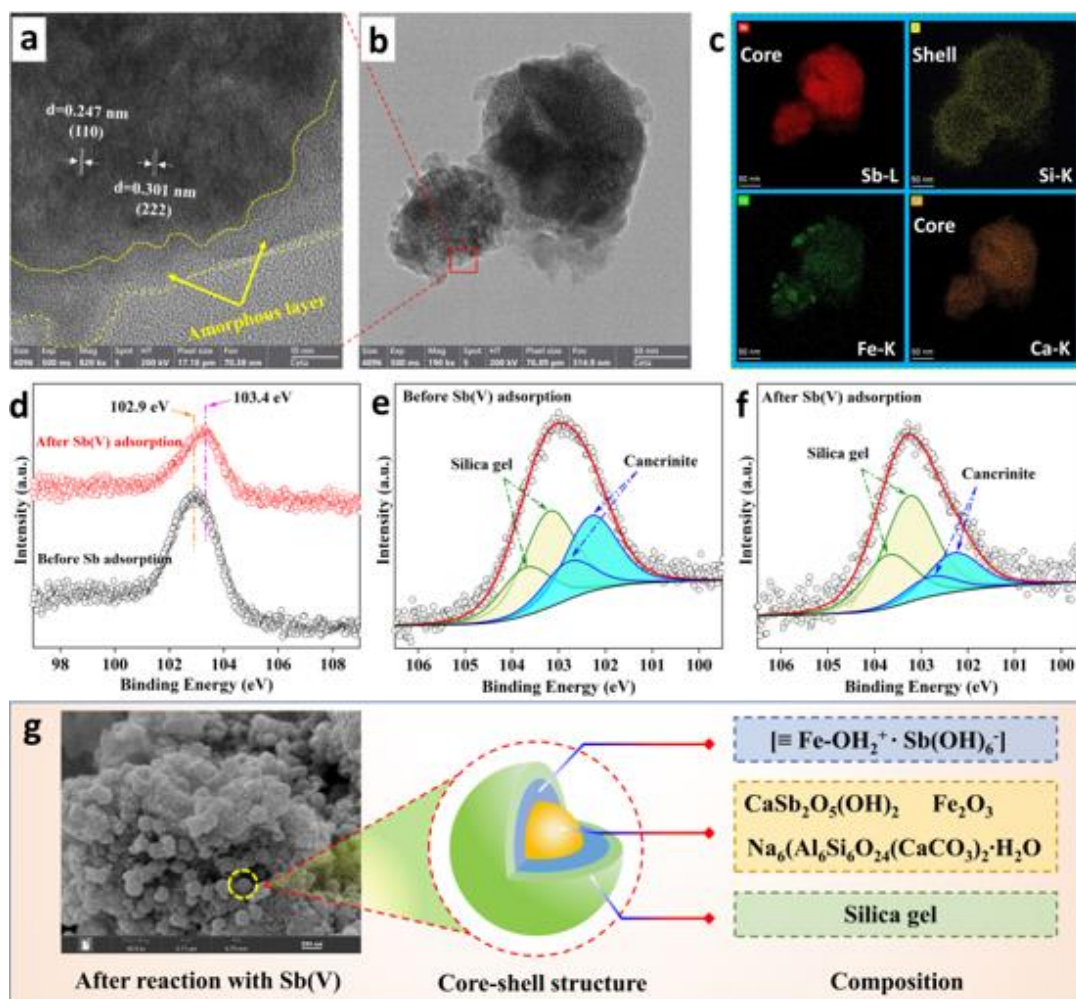


Fig. 9. (a) HRTEM, (b) TEM images, and (c) elemental mapping of the RA2 adsorbent (formed under S_{RM}/L_{AMD} of 2:1) after Sb(V) adsorption; (d-f) XPS spectra of surface Si species in the adsorbent before and after Sb(V) adsorption; (g) the structure and composition of the Sb(V)-bearing SNPs.

3.4. Adsorption of Pb onto RM-based adsorbents

3.4.1. Batch adsorption experiments

The Pb removal efficiency of the adsorbents (determined after 48 hours at pH 2.0) increased with a rising S_{RM}/L_{AMD} ratio used for the adsorbent synthesis (from 40.8% by RA2 to 90.7 % by RA10; Fig. 10a). For comparison, the original RM adsorbed only 1.9% Pb. It has been previously reported that pH can affect the adsorbent surface properties that are crucial for interactions between the adsorbent and contaminant [58]. Fig. 10b shows that the Pb removal capacity by original RM increased with rising solution pH (reaching a maximum value at pH 6), while RA10 showed a high removal capacity over the whole pH range (with a maximum at pH 5). Several studies have

reported reduced Pb removal capacity of RM and other adsorbents at acidic conditions (especially at $\text{pH} < 3$), due to the competition between H^+ and Pb(II) , together with the repulsion between the positively charged adsorbent surface and Pb(II) [59, 60]. Interestingly, the Pb removal capacity of RA10 in this study was very high even at low pH ($\sim 230 \text{ mg/g}$ at $\text{pH} 2$), which was attributed to strong chelation.

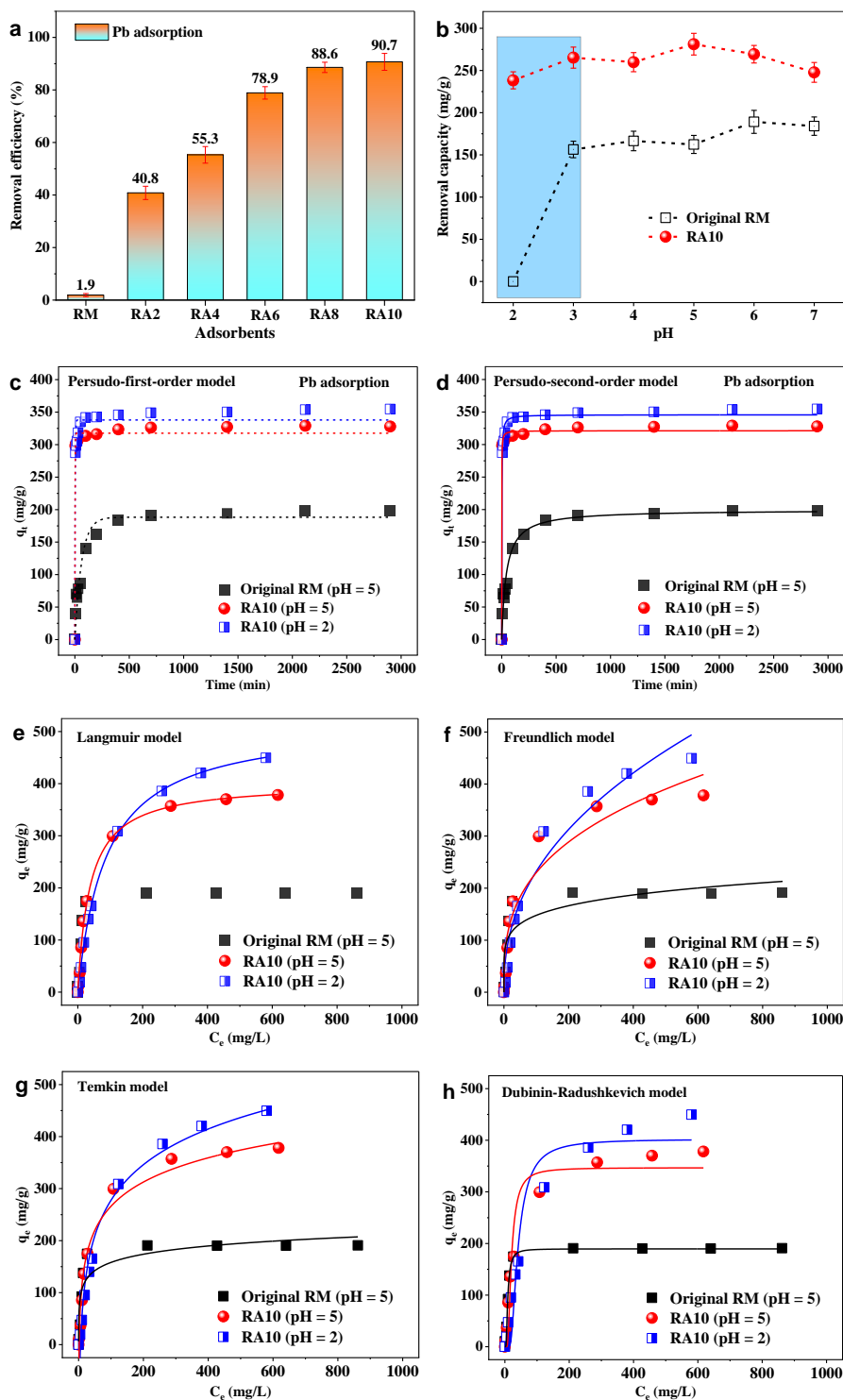


Fig. 10. (a) Removal efficiency of Pb by RM-based adsorbents synthesized under

different S_{RM}/L_{AMD} ratios; (b) Effect of pH on the removal capacity of Pb by original RM and RA10; (c, d) Adsorption kinetics and (e-h) isotherms for Pb adsorption onto the original RM and RA10 at pH 2 and 5.

3.4.2. Adsorption kinetics and isotherms using RA10 and original RM

Fig. 10c and d show that the rates of Pb adsorption by RA10 and original RM were high in the initial 100 min, and then quickly plateaued. The relation between the rate of Pb(II) adsorption (by RA10 and original RM) and contact time was analyzed using adsorption kinetic models of pseudo-first-order, pseudo-second-order, and Elovich (more in SM), together with kinetic parameters listed in Table S9. The results show that the pseudo-second-order model (giving R^2 values of 0.968, 0.995, and 0.991 for Pb(II) adsorption onto original RM at pH 5, RA10 at pH 5, and RA10 at pH 2, respectively) described the experimental data better than the two other models. Moreover, the calculated q_e values obtained from the pseudo-second-order model (198.5, 323.2, and 348.8 mg/g) were in close agreement with the experimental data (199.3, 329.0, and 354.7 mg/g, respectively). The above results indicate that the removal of Pb(II) by RA10 and original RM were controlled mainly by chemical reactions. In addition, the high R^2 value (0.976) for the Elovich model (Fig. S9, Table S9) indicated that Pb(II) could adsorb on the heterogeneous surface of RA10 at pH 5.

The Pb removal capacity of both RA10 and original RM increased with the increasing initial concentration of Pb until saturation was reached. According to the isotherm parameters of the Langmuir, Freundlich, Temkin, and Dubinin-Radushkevich models (shown in SM), the best fit to Pb adsorption onto RA10 at pH 2 and 5 was achieved with the Langmuir model ($R^2 = 0.999$ and 0.997 , respectively), while the Dubinin-Radushkevich model was the best fit for the original RM system ($R^2 = 0.990$) (Fig. 10e-h, Table S10). The above indicated that different adsorption mechanisms occurred. The maximum Pb adsorption capacities of RA10 at pH 2 and 5, and original RM at pH 5 were 518.7, 402.3, and 189.5 mg/g, respectively. Findings shown in Fig. S10 indicate the presence of Cu^{2+} and Al^{3+} lowered the efficiency of Pb(II) removal by RA10, while Zn^{2+} and Mn^{2+} had limited effects on the metal adsorption process. The comparison with other adsorbents (Table S11) shows that RM-based adsorbents modified with AMD (typically under S_{RM}/L_{AMD} ratio from 6:1 to 10:1) are low-cost sorbent materials suitable for Pb removal in a wide pH range, including low pH (< 3).

3.5. Mechanism of Pb removal

The SEM images of RA10 adsorbent after incubation with Pb(II) at pH 2 (Fig. 11a, b) showed high amounts of a relatively pure Pb compound on the adsorbent surface. The structure of this Pb compound layer was formed by thick regular polygons, which were clearly distinctive from the spherical microstructure of RA10 (Fig. 11c). The EDS element mapping images of the precipitate show that the distributions of O and S were very consistent with that of Pb (Fig. 11d). Combined with XRD results (Fig. 11e; which were similar to those obtained at pH 5, shown in Figs. 12a and S11), it was concluded that the Pb substance was PbSO_4 . Solubilization and extraction of certain elements from RA10 (especially Ca and Al; Fig. 11f) implied that ion-exchange reactions between Pb(II) and $\text{Ca}^{2+}/\text{Al}^{3+}$ occurred.

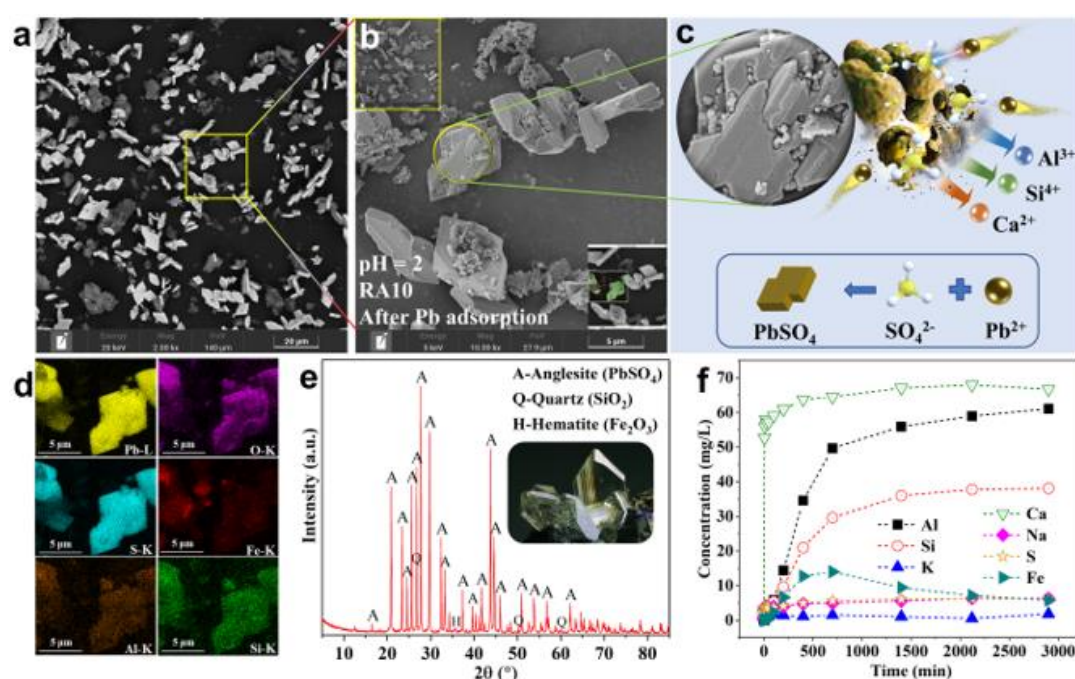


Fig. 11. (a-d) SEM-EDS images and (e) XRD pattern of the RA10 adsorbent after Pb adsorption; (f) Changes in concentrations of soluble elements from RA10 during Pb adsorption process.

No significant changes in morphology were observed on the surface of original RM after reaction with Pb(II) at pH 2, and a low Pb content (1.2 wt.%) further confirmed the negligible removal capacity of original RM (Fig. S12a). However, large amounts of PbCO_3 and $\text{Pb}_3(\text{CO}_3)_2(\text{OH})_2$ precipitates were detected on the original RM surface after Pb immobilization at pH 5 (Fig. 12b), composed mainly of (in wt.%) Pb (51.1), C (16.3), and O (23.5) (Fig. S12b).

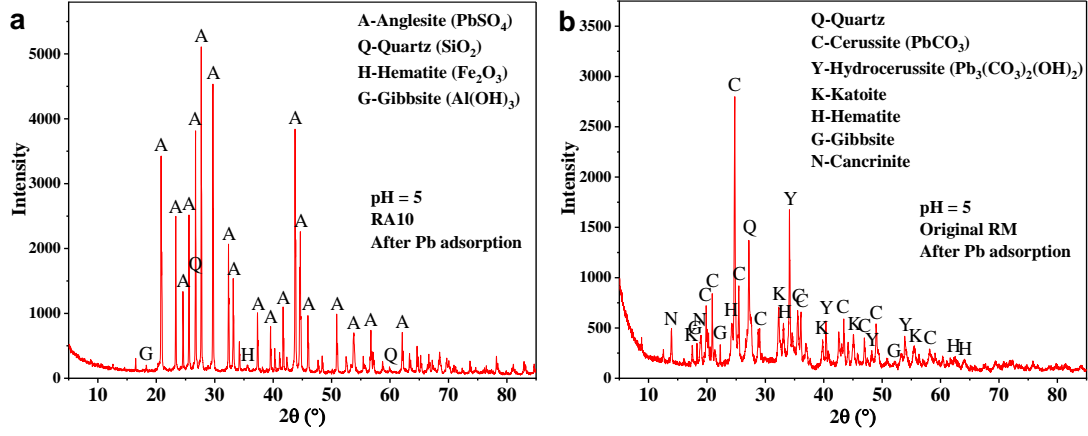
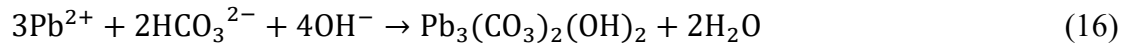


Fig. 12. XRD patterns of the (a) RA10 adsorbent and (b) original RM, after Pb adsorption at pH 5.

The mechanisms of the transformation of RA10 adsorbent and removal of Pb by RA10 and original RM have been proposed in Fig. 13. SO_4^{2-} present in AMD forms CaSO_4 and $\text{Al}_2(\text{SO}_4)_3$ on reaction with Ca and Al in RM [25]. These convertible sulfates play a dominant role in the Pb(II) removal process by RA10 via formation of PbSO_4 (Eqs. (12-14)). Of note, PbSO_4 is a major component of lead-acid batteries, and assessing the potential of the use of PbSO_4 recovered from AMD might present an interesting future research effort, which if successful would enable a transformation of industrial wastes into useful resources. In untreated RM, Pb(II) can combine with carbonate ions released from CaCO_3 and/or $\text{Na}_6(\text{Al}_6\text{Si}_6\text{O}_{24})(\text{CaCO}_3)$ phases, forming PbCO_3 (Eq. (15)) and $\text{Pb}_3(\text{CO}_3)_2(\text{OH})_2$ (Eq. (16)) precipitates (at pH 5).



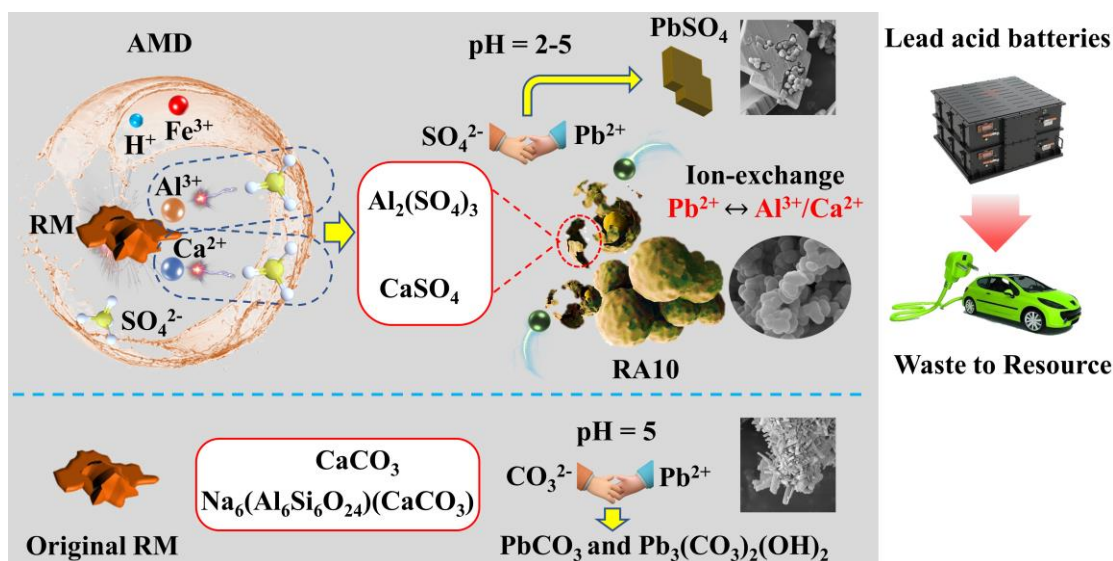


Fig. 13. Mechanisms for Pb removal by RA10 (at pH 2-5) and original RM (at pH 5).

Fig. S13 shows the efficiency of adsorption of dissolved As(III/V) and Sb(III) on to RA4 and RA2 respectively decreased only marginally after four sorption-desorption cycles, indicating a high regeneration capacity of the above adsorbents. In contrast, the efficiency of Sb(V) and Pb(II) removal by RA2 and RA10 respectively decreased sharply after the first experiment cycle. This was ascribed to the formation of large amounts of $\text{CaSb}_2\text{O}_5(\text{OH})_2$ and PbSO_4 precipitates, which consequently led to irreversible transformations and reduced regeneration capacity of RA2 (Fig. 7c) and RA10 (Fig. 11e) after adsorption of Sb(V) and Pb(II) respectively. The above implies that As(III/V) and Sb(III) removal from solution was mainly via adsorption, while chemical co-precipitation and ion-exchange reactions were involved in Sb(V) and Pb(II) immobilization processes.

The above results also indicate that H^+ and especially Fe^{3+} in AMD were the main factors that drove RM dissolution and transformation via neutralization and ion-exchange reactions between Fe^{3+} (in AMD) and Al/Si/Ca/K/Na (in RM), respectively. Surface $\equiv\text{Fe}-\text{OH}$ in RA4 played a dominant role in the adsorption of negatively charged As(V), while primarily Ca^{2+} in RA2 contributed to the removal of Sb(V) via the formation of $\text{CaSb}_2\text{O}_5(\text{OH})_2$. At low pH, As(III) and Sb(III) exist predominantly in the form of H_3AsO_3 and $[\text{Sb}(\text{OH})_3]^0$ [31, 61]. These species proved difficult to be oxidized (to H_2AsO_4^- and $[\text{Sb}(\text{OH})_6]^-$ respectively) by Fe(III)-rich RA4 or RA2 in this study, which consequently reduced the efficiency of their removal from solution. In contrast to As and Sb removal, SO_4^{2-} in AMD played a major role in Pb(II) removal. This process

proceeded first via a reaction with RM to form convertible sulfates (i.e., CaSO_4 and $\text{Al}_2(\text{SO}_4)_3$ in RA10), followed by a reaction with Pb(II) to form a PbSO_4 precipitate. Lower ratios of $S_{\text{RM}}/L_{\text{AMD}}$ ($\leq 4:1$) resulted in greater dissolution of RM and higher contents of Fe(III) on the adsorbent surfaces, which promoted the rates of removal of negatively charged As (V) and Sb (V). An elevated $S_{\text{RM}}/L_{\text{AMD}}$ ratio, on the other hand, promoted sulfate formation and lowered the concentration of Fe (III) on the adsorbent surface, which promoted the immobilization of positively charged Pb(II).

4. Conclusions

This work presents a novel approach to resource utilization, providing a cost-effective way to produce an adsorbent for efficient As, Sb, and Pb removal from acidic waters, using two industrial wastes that are generated and accumulate in large quantities. The main findings are summarized below:

(1) Fe(III), H^+ , and SO_4^{2-} in AMD can effectively drive the dissolution and transformation of RM via neutralization and ion-exchange reactions. The $S_{\text{RM}}/L_{\text{AMD}}$ ratio significantly affects the structure and composition of the adsorbent. RA2, RA4, and RA10 adsorbents exhibited the greatest removal capacity for Sb, As, and Pb respectively.

(2) Removal of Sb(V/III), As(V), and Pb(II) using RA2, RA4, and RA10 follows the Langmuir isotherm model, whereas the processes of removal of As(III) by RA4 and of Pb(II) by untreated RM follow the Freundlich and Dubinin-Radushkevich isotherm models, respectively. At pH 2, the maximum removal capacities for Sb(V), Sb(III), As(V), As(III), and Pb(II) were 1,637.8, 80.2, 109.2, 16.4, and 518.7 mg/g, respectively.

(3) Fe(III) (hydr)oxides (e.g., FeOOH and $\text{Fe}(\text{OH})_3$) formed via reactions between RM and AMD played a dominant role in As(V) adsorption. As-K-EXAFS measurements indicated that As(V) formed complexes with Fe/Al-bearing compounds in RA4. Besides Fe(III) hydroxyl groups, Ca^{2+} significantly contributed to Sb(V) immobilization via the formation of $\text{CaSb}_2\text{O}_5(\text{OH})_2$. The silica gel attached to the surface enhanced the stability of the Sb-bearing precipitate.

(4) RA10 adsorbent exhibited an excellent Pb removal capacity across a wide range of pH (including values as low as pH 2), and convertible sulfates (e.g., CaSO_4 and

$\text{Al}_2(\text{SO}_4)_3$) formed via reactions between AMD and RM played a key role in the PbSO_4 precipitation process. On the other hand, the formation of PbCO_3 and $\text{Pb}_3(\text{CO}_3)_2(\text{OH})_2$ was the main Pb(II) removal mechanism by untreated RM, determined at pH 5 (while no Pb(II) adsorption by original RM was observed at pH 2).

Acknowledgements

This work was supported by the National Natural Science Foundation of China (grants No. 51861135305 and 41830318). We would like to thank Tie-Fu Xu (Hunan Navi New Material Technology Co., Ltd.) for his assistance in micromorphology analysis.

References

- [1] Antoniadis, V., Golia, E.E., Liu, Y.-T., Wang, S.-L., Shaheen, S.M., Rinklebe, J., 2019. Soil and maize contamination by trace elements and associated health risk assessment in the industrial area of Volos, Greece. *Environ. Int.* 124, 79-88.
- [2] Islam, M.R., Khan, I., Attia, J., Hassan, S.M.N., McEvoy, M., D'Este, C., Azim, S., Akhter, A., Akter, S., Shahidullah, S.M., Milton, A.H., 2012. Association between hypertension and chronic arsenic exposure in drinking water: A cross-sectional study in Bangladesh. *Int J Environ Res Public Health.* 9, 4522-4536.
- [3] Ungureanu, G., Santos, S., Boaventura, R., Botelho, C., 2015. Arsenic and antimony in water and wastewater: overview of removal techniques with special reference to latest advances in adsorption. *J. Environ. Manage.* 151, 326-342.
- [4] Ritchie, V.J., Ilgen, A.G., Mueller, S.H., Trainor, T.P., Goldfarb, R.J., 2013. Mobility and chemical fate of antimony and arsenic in historic mining environments of the Kantishna Hills district, Denali National Park and Preserve, Alaska. *Chem. Geol.* 335, 172-188.
- [5] Carter, J.A., Erhardt, R.J., Jones, B.T., Donati, G.L., 2020. Survey of lead in drinking water from schools and child care centers operating as public water suppliers in North Carolina, USA: implications for future legislation. *Environ. Sci. Technol.* 54, 14152-14160.
- [6] Khalid, S., Shahid, M., Dumat, C., Niazi, N.K., Bibi, I., Gul Bakhat, H.F.S., Abbas, G., Murtaza, B., Javeed, H.M.R., 2017. Influence of groundwater and wastewater

irrigation on lead accumulation in soil and vegetables: implications for health risk assessment and phytoremediation. *Int. J. Phytoremediation* 19, 1037-1046.

[7] Ullah, S., Iqbal, Z., Mahmood, S., Akhtar, K., Ali, R., 2020. Phytoextraction potential of different grasses for the uptake of cadmium and lead from industrial wastewater. *Soil Environ.* 39, 77-86.

[8] Sarkar, A., Paul, B., 2016. The global menace of arsenic and its conventional remediation-a critical review. *Chemosphere* 158, 37-49.

[9] Nazari, A.M. Radzinski, R., Ghahreman, A., 2017. Review of arsenic metallurgy: Treatment of arsenical minerals and the immobilization of arsenic, *Hydrometallurgy*. 174, 258-281.

[10] Chi, Z., Ju, S., Liu, X., Sun, F., Zhu, Y., 2022. Graphene oxide supported sulfidated nano zero-valent iron (S-nZVI@GO) for antimony removal: The role of active oxygen species and reaction mechanism. *Chemosphere* 308, 136253.

[11] Yuan, Z., Zhang, G., Lin, J., Zeng, X., Ma, X., Wang, X., Wang, S., Jia, Y., 2019. The stability of Fe(III)-As(V) co-precipitate in the presence of ascorbic acid: effect of pH and Fe/As molar ratio. *Chemosphere* 218, 670-679.

[12] Du, X., Qu, F., Liang, H., Li, K., Yu, H., Bai L., Li, G., 2014. Removal of antimony (III) from polluted surface water using a hybrid coagulation-flocculation-ultrafiltration (CF-UF) process. *Chem. Eng. J.* 254, 293-301.

[13] Yan, L., Yin, H.H., Zhang, S., Leng, F.F., Nan, W.B., Li, H.Y., 2010. Biosorption of inorganic and organic arsenic from aqueous solution by *Acidithiobacillus ferrooxidans* BY-3. *J. Hazard. Mater.* 178, 209-217.

[14] Kumar, P.S., Gayathri, R., Rathi, B.S., 2021. A review on adsorptive separation of toxic metals from aquatic system using biochar produced from agro-waste. *Chemosphere* 285, 131438.

[15] Adamczuk, A., Kołodyńska, D., 2015. Equilibrium, thermodynamic and kinetic studies on removal of chromium, copper, zinc and As from aqueous solutions onto fly ash coated by chitosan. *Chem. Eng. J.* 274, 200-212.

[16] Agrawal, S., Dhawan, N., 2021. Evaluation of red mud as a polymetallic source-A

review, *Miner. Eng.* 171, 107084.

[17] Yang, D.Z., Deng, W.W., Tan, A., Chu, Z.T., Wei, W.F., Zheng, R.J., Shangguan, Y.Z., Sasaki, A., Endo, M., Chen, H., 2021. Protonation stabilized high As/F mobility red mud for Pb/As polluted soil remediation. *J. Hazard. Mater.* 404, 124143.

[18] Liu, X., Han, Y.X., He, F.Y., Gao, P., Yuan, S., 2021. Characteristic, hazard and iron recovery technology of red mud-A critical review. *J. Hazard. Mater.* 420, 126542.

[19] Akin I., Arslan G., Tor A., Ersoz M., Cengeloglu Y., 2012. Arsenic(V) removal from underground water by magnetic nanoparticles synthesized from waste red mud. *J. Hazard. Mater.* 235-236, 62-68.

[20] Carvalheiras, J., Novais, R.M., Labrincha, J.A., 2023. Metakaolin/red mud-derived geopolymer monoliths: Novel bulk-type sorbents for lead removal from wastewaters. *Appl Clay Sci.* 232, 106770.

[21] Lyu, F., Niu, S., Wang, L., Liu, R., Sun, W., He, D., 2021. Efficient removal of Pb(II) ions from aqueous solution by modified red mud. *J. Hazard. Mater.* 406, 124678.

[22] Tabelin, C.B., Corpuz, R.D., Igarashi, T., Villacorte-Tabelin, M., Alorro, R.D., Yoo, K., Raval, S., Ito, M., Hiroyoshi, N., 2020. Acid mine drainage formation and arsenic mobility under strongly acidic conditions: Importance of soluble phases, iron oxyhydroxides/oxides and nature of oxidation layer on pyrite. *J. Hazard. Mater.* 399, 122844.

[23] Huang, A., Zhi, D., Tang, H., Jiang, L., Luo, S., Zhou, Y., 2020. Effect of Fe²⁺, Mn²⁺ catalysts on the performance of electro-Fenton degradation of antibiotic ciprofloxacin, and expanding the utilizing of acid mine drainage. *Sci. Total Environ.* 720, 137560.

[24] Sun, Y.M., Zhai, L.F., Duan, M.F., Sun, M., 2018. In Situ Fabrication of Electro-Fenton Catalyst from Fe²⁺ in Acid Mine Drainage: Influence of Coexisting Metal Cations. *ACS Sustain. Chem. Eng.* 6, 14154-14161.

[25] Chen, H.R., Zhang, D.R., Li, Q., Nie, Z.Y., Pakostova, E., 2022. Release and fate of As mobilized via bio-oxidation of arsenopyrite in acid mine drainage: Importance of As/Fe/S speciation and As (III) immobilization. *Water Res.* 223, 118957.

- [26] Chen, M., Lu, G., Wu, J., Sun, J., Dang, Z., 2020. Acidity and metallic elements release from AMD-affected river sediments: effect of AMD standstill and dilution. *Environ. Res.* 186, 109490.
- [27] Yin, H., Kwon, K.D., Lee, J.Y., Shen, Y., Zhao, H., Wang, X., Liu, F., Zhang, J., Feng, X., 2017. Distinct effects of Al³⁺ doping on the structure and properties of hexagonal turbostratic birnessite: a comparison with Fe³⁺ doping. *Geochem. Cosmochim. Acta* 208, 268-284.
- [28] Ravel, B., Newville, M., 2005. ATHENA, ARTEMIS, HEPHAESTUS: data analysis for X-ray absorption spectroscopy using IFEFFIT. *J. Synchrotron Radiat.* 12, 537-541.
- [29] Zhang, D.R., Chen, H.R., Zhao, X.J., Nie, Z.Y., Xia, J.L., Li, E.P., Fan, X.L., Zheng, L., 2020. Extraction of Al and rare earths (Ce, Gd, Sc, Y) from red mud by aerobic and anaerobic bi-stage bioleaching. *Chem. Eng. J.* 401, 125914.
- [30] Agatzini-Leonardou, S., Oustadakis, P., Tsakiridis, P., Markopoulos, C., 2008. Titanium leaching from red mud by diluted sulfuric acid at atmospheric pressure. *J. Hazard. Mater.* 157, 579-586.
- [31] Cheng, H., Hu, Y., Luo, J., Xu, B., Zhao, J., 2009. Geochemical processes controlling fate and transport of arsenic in acid mine drainage (AMD) and natural systems. *J. Hazard. Mater.* 165, 13-26.
- [32] Kim, H.J., Kim, Y., 2021. Schwertmannite transformation to goethite and the related mobility of trace metals in acid mine drainage. *Chemosphere* 269, 128720.
- [33] Jönsson, J., Jönsson, J., Lövgren L., 2006. Precipitation of secondary Fe(III) minerals from acid mine drainage. *Appl. Geochem.* 21, 437-445.
- [34] Lu, J., Wen, Z., Zhang, Y., Cheng, G., Xu, R., Gong, X., Wang, X., Chen, R., 2021. New insights on nanostructure of ordered mesoporous Fe-Mn bimetal oxides (OMFMs) by a novel inverse micelle method and their superior arsenic sequestration performance: effect of calcination temperature and role of Fe/Mn oxides. *Sci. Total Environ.* 762, 143163.
- [35] Ge, X., Liu, J., Song, X., Wang, G., Zhang, H., Zhang, Y., Zhao, H., 2016.

Hierarchical iron containing γ -MnO₂ hollow microspheres: a facile one-step synthesis and effective removal of As(III) via oxidation and adsorption. *Chem. Eng. J.* 301, 139-148.

[36] Luo, J., Luo, X., Crittenden, J., Qu, J., Bai, Y., Peng, Y., Li, J., 2015. Removal of antimonite (Sb(III)) and antimonate (Sb(V)) from aqueous solution using carbon nanofibers that are decorated with zirconium oxide (ZrO₂). *Environ. Sci. Technol.* 49, 11115-11124.

[37] Langmuir, I., 1918. The adsorption of gases on plane surfaces of glass, mica and platinum. *J. Am. Chem. Soc.* 40, 1361-1403.

[38] Freundlich, H.M.F., 1906. Über die adsorption in Lösungen. *Z. Phys. Chem.* 5, 385-470.

[39] Soltani, R., Marjani, A., Shirazian, S., 2019. Facile one-pot synthesis of thiol-functionalized mesoporous silica submicrospheres for Tl(I) adsorption: isotherm, kinetic and thermodynamic studies. *J. Hazard. Mater.* 371, 146-155.

[40] Li, Q., Ma, X.Y., Qi, C.S., Li, R., Zhang, W., Li, J.S., Shen, J.Y., Sun, X.Y., 2022. Facile preparation of novel magnetic mesoporous FeMn binary oxides from Mn encapsulated carboxymethyl cellulose-Fe(III) hydrogel for antimony removal from water. *Sci. Total Environ.* 821, 153529.

[41] Igarashi, T., Herrera, P.S., Uchiyama, H., Miyamae, H., Iyatomi, N., Hashimoto, K., Tabelin, C.B., 2020. The two-step neutralization ferrite-formation process for sustainable acid mine drainage treatment: removal of copper, zinc and arsenic, and the influence of coexisting ions on ferritization. *Sci. Total Environ.* 715, 136877.

[42] Carrero, S., Fernandez-Martinez, A., Pérez-López, R., Poulain, A., Salas-Colera, E., Nieto, J. M., 2016. Arsenate and selenate scavenging by basaluminite: insights into the reactivity of aluminum phases in acid mine drainage. *Environ. Sci. Technol.* 51, 28-37.

[43] Zhang, G.S., Qu, J.H., Liu, H.J., Liu, R.P., Li, G.T., 2007. Removal mechanism of As(III) by a novel Fe-Mn binary oxide adsorbent: Oxidation and sorption. *Environ. Sci. Technol.* 41, 4613-4619.

[44] Yang, K., Zhou, J., Lou, Z., Zhou, X., Liu, Y., Li, Y., Baig, S.A., Xu, X., 2018.

Removal of Sb(V) from aqueous solutions using Fe-Mn binary oxides: the influence of iron oxides forms and the role of manganese oxides. *Chem. Eng. J.* 354, 577-588.

[45] Herranz, T., Rojas, S., Ojeda, M., Perez-Alonso, F.J., Terreros, P., Pirota, K., Fierro, J.L.G., 2006. Synthesis, structural features, and reactivity of Fe-Mn mixed oxides prepared by microemulsion. *Chem. Mater.* 18, 2364-2375.

[46] Nesbitt, H.W., Muir, I.J., 1998. Oxidation states and speciation of secondary products on pyrite and arsenopyrite reacted with mine waste waters and air. *Miner. Petrol.* 62, 123-144.

[47] Le Berre, J.F., Gauvin, R., Demopoulos, G.P., 2008. A study of the crystallization kinetics of scorodite via the transformation of poorly crystalline ferric arsenate in weakly acidic solution. *Colloids and Surfaces A: Physicochem. Eng. Aspects* 315, 117-129.

[48] Lee, S.Y., Chang, B., Kim, Y.J., Jang, H., Lee, Y.J., 2022. Characterization of arsenite (As(III)) and arsenate (As(V)) sorption on synthetic siderite spherules under anoxic conditions: Different sorption behaviors with crystal size and arsenic species. *J. Colloid Interface Sci.* 613, 499-514.

[49] ONA-Nguema, G., Morin, G., Juillot, F., Calas, G., Jr, G.E.B., 2005. EXAFS analysis of arsenite adsorption onto two-line ferrihydrite, hematite, goethite, and lepidocrocite. *Environ. Sci. Technol.* 39, 9147-9155.

[50] Pinakidou, F., Katsikini, M., Simeonidis, K., Paloura, E.C., Mitrakas, M., 2015. An X-ray absorption study of synthesis- and As adsorption-induced microstructural modifications in Fe oxy-hydroxides. *J. Hazard. Mater.* 298, 203-209.

[51] Kappen, P and Webb, J., 2013. An EXAFS study of arsenic bonding on amorphous aluminium hydroxide. *Appl. Geochem.* 31, 79-83.

[52] Van Caneghem, J., Verbinnen, B., Cornelis, G., Wijs, J., Mulder, R., Billen, P., Vandecasteele, C., 2016. Immobilization of antimony in waste-to-energy bottom ash by addition of calcium and iron containing additives. *Waste Manage.* 54, 162-168.

[53] Huang, R., Xu, X., Zhu, J, Liu, W., Yuan, R., Fu, X., Zhang, Y., 2012. Nanocrystalline $\text{CaSb}_2\text{O}_5(\text{OH})_2$ and $\text{Ca}_2\text{Sb}_2\text{O}_7$: Controlled syntheses, electronic

- structures and photocatalytic activity. *Appl. Catal. B: Environ.* 127, 205-211.
- [54] Mishra, S., Dwivedi, J., Kumar, A., Sankararamakrishnan, N., 2016. Removal of antimonite (Sb(III)) and antimonate (Sb(V)) using zerovalent iron decorated functionalized carbon nanotubes. *RSC Adv.* 6, 95865-9587.
- [55] Wang, L., Wan, C.L., Zhang, Y., Lee, D.J., Liu, X., Chen, X.F., Tay, J.H., 2015. Mechanism of enhanced Sb(V) removal from aqueous solution using chemically modified aerobic granules. *J. Hazard. Mater.* 284, 43-49.
- [56] Zhou, L., Li, A., Ma, F., Zhao, H., Deng, F., Pi, S., Tang, A., Yang, J., 2020. Combining high electron transfer efficiency and oxidation resistance in nZVI with coatings of microbial extracellular polymeric substances to enhance Sb(V) reduction and adsorption. *Chem. Eng. J.* 395, 125168.
- [57] Wagner, C., Passoja, D., Hillery, H., Kinisky, T., Six, H., Jansen, W., Taylor, J., 1982. Auger and photoelectron line energy relationships in aluminum-oxygen and silicon-oxygen compounds. *J. Vac. Sci. Technol.* 21, 933-944.
- [58] Kamboh, M.A., Wan Ibrahim, W.A., Nodeh, H.R., Sanagi, M.M., Sherazi, S.T.H., 2016. The removal of organophosphorus pesticides from water using a new amino-substituted calixarene-based magnetic sporopollenin. *New J. Chem.* 40, 3130-3138.
- [59] Mosleh, N., Najmi, M., Parandi, E., Nodeh, H., Vasseghian, Y., Rezaia, S., 2022. Magnetic sporopollenin supported polyaniline developed for removal of lead ions from wastewater: Kinetic, isotherm and thermodynamic studies. *Chemosphere* 300, 134461.
- [60] Manawi, Y., McKay, G., Ismail, N., Fard, A.K., Kochkodan, V., Atieh, M.A., 2018. Enhancing lead removal from water by complex-assisted filtration with acacia gum. *Chem. Eng. J.* 352, 828-836.
- [61] Herath, I., Vithanage, M., Bundschuh, J., 2017. Antimony as a global dilemma: geochemistry, mobility, fate and transport. *Environ. Pollut.* 223, 545-559.